Computational Study of Inertial Migration of Prolate Particles in a Straight Rectangular Channel

BY

GIUSEPPE LAURICELLA
M.S., Politecnico di Milano, Milan, Italy, 2022

THESIS

Submitted as partial fulfillment of the requirements
for the degree of Master of Science in Biomedical Engineering
in the Graduate College of the
University of Illinois at Chicago, 2023

Chicago, Illinois

Defense Committee:

Zhangli Peng, Chair and Advisor

Ian Papautsky, Co-Advisor

Guido Raos, Politecnico di Milano

ACKNOWLEDGMENTS

I thank Profs. Peng and Papautsky for their constant and essential support since the very beginning of this journey, and Professor Raos for assisting me in the discussion of the work. The thesis is based on the article published on *Physics of Fluids* with the title "Computational study of inertial migration of prolate particles in a straight rectangular channel". I would like to acknowledge the other authors of the manuscript: Jian Zhou, Qiyue Luan, Ian Papautsky, and Zhangli Peng.

The work received partial support from the National Science Foundation and the industrial members of the Center for Advanced Design and Manufacturing of Integrated Microfluidics (NSF I/UCRC award IIP- 1841473). Further support was provided by NSF/DMS 1951526. The simulations were conducted on the supercomputer Theta in Argonne Leadership Computing Facility (ALCF) in the Argonne National Lab under Director's Discretionary (DD) allocation Modeling Corona Virus. This research used resources of the Argonne Leadership Computing Facility, which is a DOE Office of Science User Facility supported under Contract DE-AC02-06CH11357.

GL

ACKNOWLEDGMENTS (continued)

CONTRIBUTION OF AUTHORS

Chapter 1 is a broad insight into the fundamentals of this work, namely inertial microfluidics and computational fluid dynamics. A quick overview of the most common numerical methods involved in this area of research is presented. Chapter 2 is more specific about the numerical method that I have used in this work to perform the microfluidic investigation. All the tools that have been used to obtain and post-process the results are also presented in this section. The experimental methods present in Chapter 2 have been provided by Jian Zhou. Chapter 3 summarized the main results and part of it is also present in a published manuscript (Lauricella, Giuseppe, et al. "Computational study of inertial migration of prolate particles in a straight rectangular channel." Physics of Fluids 34.8 (2022): 082021) for which I was the primary author and major driver of the research. Ian Papautsky, Jian Zhou, and Qiyue Luan provided me with the experimental results partially shown in Figure 7. Conclusions and future directions are addressed in Chapter 4.

TABLE OF CONTENTS

TABLE OF CONTENTS (continued)

CHAPTER **PAGE**

LIST OF TABLES

LIST OF FIGURES

LIST OF FIGURES (continued)

LIST OF ABBREVIATIONS

ALCF	Argonne Leadership Computing Facility
ALE	Arbitrary Lagrangian-Eulerian Method
AR	Aspect Ratio
BVP	Boundary Value Problem
CFD	Computational Fluid Dynamics
CHARMM	Chemistry at Harvard Macromolecular Mechanics
COM	Center of Mass
CPU	Central Processing Unit
CTC	Circulating Tumor Cell
DEM	Diffuse Element Method
DLD	Deterministic Lateral Displacement
DNS	Direct Numerical Simulation
DPD	Dissipative Particle Dynamics
EAM	Embedded Atom Method
EFG	Element Free Galerkin
EOS	Equation of State
FSPP	Flow at Specific Particle Position

LIST OF ABBREVIATIONS (continued)

GPU	Graphics Processing Unit
GROMACS	GROningen MAchine for Chemical Simulation
HDF	Hydrodynamic Filtration
IBM	Immersed Boundary Method
ISPH	Incompressible SPH
IVP	Initial Value Problem
LAMMPS	Large-scale Atomic Molecular Massively Parallel Simulator
LBGK	Lattice Bhatnagar-Gross-Krook
LBM	Lattice Boltzmann Method
LGA	Lattice Gas Automata
MD	Molecular Dynamics
MIMD	Multiple Instructions Multiple Data
MISD	Multiple Instructions Single Data
MPI	Message Passing Interface
MSTR	Mirror Symmetry Time Reversal
MWS	Mesh-free Weak-Strong
NAMD	NAnoscale Molecular Dynamics
NSCLC	Non-Small-Cell-Lung Cancer

LIST OF ABBREVIATIONS (continued)

ODE	Ordinary Differential Equation
PBC	Periodic Boundary Condition
PCR	Polymerase Chain Reaction
PDE	Partial Differential Equation
PDMS	PolyDiMethylSiloxane
PFF	Pinched-Flow Fractionation
PIM	Point Interpolation Method
PME	Particle-Mesh Ewald
PPE	Pressure Poisson's Equation
RBC	Red Blood Cell
RM	Rotational Mode
SIMD	Single Instruction Multiple Data
SISD	Single Instruction Single Data
SPH	Smoothed Particle Hydrodynamics
SP	Starting Position
VMD	Visual Molecular Dynamics
WBC	White Blood Cell
WCSPH	Weakly-Compressible SPH

SUMMARY

Inertial migration of spherical particles has been investigated extensively using experiments, theory, and computational modeling. Yet, a systematic investigation of the effect of particle shape on inertial migration is still lacking. Herein, we numerically mapped the migration dynamics of a prolate particle in a straight rectangular microchannel using smoothed particles hydrodynamics (SPH), at moderate Reynolds number flows. After validations, we applied our model to 2:1 and 3:1 shape aspect ratio particles at multiple confinement ratios. Their effects on the final focusing position, rotational behavior, and transitional dynamics were studied. In addition to the commonly reported tumbling motion, for the first time, we identified a new logrolling behavior of a prolate ellipsoidal particle in the confined channel. This new behavior occurs when the confinement ratio is above a threshold value of K = 0.72. Microfluidic experiments using cell aggregates with similar shape aspect ratio and confinement ratio confirmed this new predicted logrolling motion. We also found that the same particle can undergo different rotational modes, including kayaking behavior, depending on its initial cross-sectional position and orientation. Furthermore, we examined the migration speed, angular velocity, and rotation period, as well as their dependence on both particle shape aspect ratio and confinement ratio. The computational model we developed in the present work can be extended to study other shapes, channel geometries, and flow conditions. Our findings are especially relevant to the applications where particle shape and alignment are used for sorting and analysis, such as the

use of barcoded particles for biochemical assays through optical reading, or the shape-based enrichment of microalgae, bacteria, and chromosomes.

CHAPTER 1

BACKGROUND

In the past decade, inertial microfluidics has gained popularity among the different techniques to separate and sort cells and particles at the microscale [3]. It is particularly suitable for biological and medical applications since it solely relies on the effect of fluid inertia [4]. The majority of studies on inertial migration have focused on spherical particles, and there is a lack of experimental and computational studies on shaped particles [5] due to the associated technical challenges. Shaped particles are difficult to manufacture and their complex dynamics make their simulations computationally expensive. Common non-spherical particles include ellipsoids, such as prolate (λ = radial diameter/equatorial diameter > 1) and oblate ($\lambda < 1$), non-ellipsoids, such as rod-like and disk-shaped beads, and asymmetric particles. Cells found in biological samples are best represented by deformable spherical particles, capable of changing their morphology, thus shape could be used to distinguish between different cell types, cell states, and cell cycle stages.

In this work, we systematically explored the inertial migration dynamic behavior of prolate particles in a straight rectangular microchannel. We numerically investigated the effects of different shape aspect ratios and confinement ratios using smoothed particles hydrodynamics (SPH) [6]. Our computational study serves as the first systematic investigation of the inertial migration behavior of prolate particles in a microchannel. In the following sections, a description of inertial microfluidics will be provided, followed by the current state of the art, with a specific

focus on shaped-particles. Then, a brief overview of numerical analysis will be given, followed by the computational modeling of inertial microfluidics. The Methods section will mainly cover a description of SPH and its implementation. Next, the results will be presented and discussed. Lastly, in the Conclusions section, the final remarks and future perspectives will be addressed.

1.1 Inertial microfluidics

Microfluidics is the area of research devoted to the manipulation of fluids in micro channels and it has experienced a massive development in the past decade. The purpose of microfluidic devices is to mix or separate particles or fluids, in a cheap, fast and portable way. Particles include cells and biological specimens. The enrichment and sorting of particles can be obtained by applying an external force field or exploiting passive hydrodynamic forces. Many microfluidic devices employ external forces, using either an electromagnetic field [7, 8], acoustic field [9], or light field [10]. However, they could result in damage to the biological particles that are being analyzed. These sorting methods are classified as active microfluidics. In addition to these techniques, separation can be also achieved by exploiting the fluid properties, channel geometry, the particle morphology and its interaction with posts and walls. Some examples include hydrodynamic filtration (HDF), deterministic lateral displacement (DLD), pinched-flow fractionation (PFF), and gravitational methods [11, 12].

Most of the previous separation methods operate in Stokes regime, where the characteristic Reynolds number of the flow is smaller than one. The Reynolds number Re represents the ratio of inertial to viscous forces

$$Re = \frac{vD_h\rho}{\mu} \tag{1.1}$$

where v is the average velocity of the fluid, D_h is the hydraulic diameter of the channel, ρ and μ are the fluid density and viscosity, respectively. If $Re << 1$, it means that the effect of inertia is negligible. The low velocity of the flow is responsible for the low throughput of these devices. Considering also their design complexity, their use for industrial scale applications is hindered [13].

Inertial microfluidics exploits fluid inertia in confined channel flows, where the Reynolds number is typically in the range of 1-100, and the laminar flow regime is ensured. Brownian motion is negligible in this range of applications. Since inertia is not zero, in a straight channel with either a square or a rectangular cross-section, particles are subjected to inertial lift forces. When the forces are balanced, a stable equilibrium position for a particle can be achieved [14]. The current understanding of the physics underlying this phenomenon is based on the two main forces acting on a spherical particle – the shear gradient-induced lift force and the wall-induced lift force [15], that will be described later on. Besides these, in specific cases, such as spiral channels, other secondary lift forces take place and further influence the final equilibrium position of the particle. In general, several variables affect the inertial migration of a particle, and these include flow parameters, types of channel cross-sections and geometries, and particle and suspension characteristics. Rapid prototyping allows to explore a variety of channel geometries, such as straight, curving, spiral, that can be used with different cross-sections, such as square, circular, rectangular, and triangular.

In a straight channel with rectangular cross-section, there are typically two stable equilibrium positions located close to the longer channel walls, at the center mid-line, as shown in Figure 1.

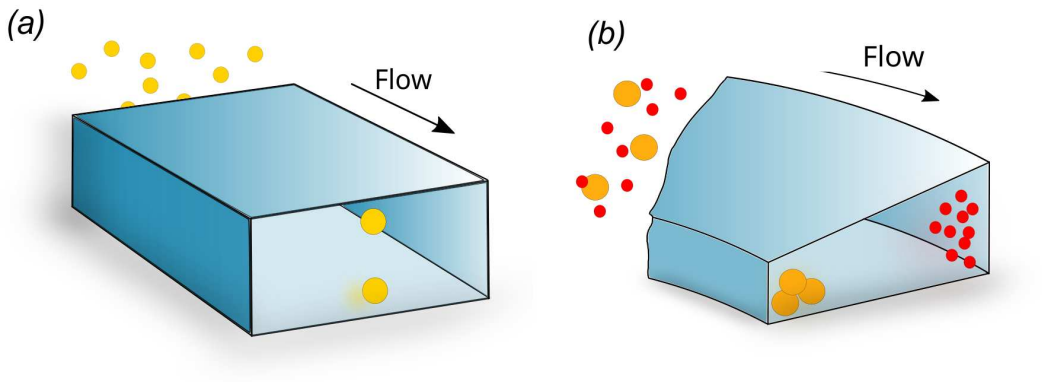

Figure 1: (a) Straight rectangular channel where the particles focus at the top and bottom of the cross-section's center-line. (b) Portion of a spiral channel with trapezoidal cross-section. The presence of secondary flows drives bigger particles close to the inner part of the channel and smaller particles move towards the outer region of the channel.

The inertial migration of particles in a microchannel was first reported in 1961 by Segre and Silberberg [16]. They observed that, in a circular pipe, it was possible to collect spherical particles in an annular region located at a distance 0.6 times the radius length, away from the center. A lot of theoretical, experimental and numerical studies followed this first observation, and they allowed to gain a better understanding of this phenomenon, even though there is still a lot to be clarified and discovered.

1.1.1 Physics of inertial microfluidics

One of the main characteristics of inertial microfluidics is the laminarity of the flow. If a particle moves downstream in a microchannel and no external forces are applied, it will follow the fluid streamlines. In fluid mechanics, a flow streamline is a path that goes along with the

velocity vector field, that an ideal massless particle would follow. When the Reynolds number of the channel increases, inertial forces prevail over viscous forces, and the migration of particles across streamlines is observed [17].

Inertial forces are classified as dominant and weak lift forces. The dominant inertial lift forces include:

1. The **wall-induced** lift force, directing the particles away from the wall. The effect of walls in a confined flow is different from that in an unbounded flow. If a particle is sufficiently close to a wall, the primary effect it experiences is a deceleration, and then it is driven away from the wall, towards the channel centerline;
2. The **shear gradient induced** lift force, which pushes the particles towards the walls. It is due to the curvature of the fluid velocity profile. In general, when there is no curvature, it is referred as a simple shear flow. Inside a channel, the presence of the curvature directs the particle away from the center of the channel;
3. The **rotation-induced** lift force, introduced for the first time in the two-stage model by Zhou and Papautsky [18]. In this model, the particle migrates towards the nearest wall in the first stage. The main driving force is the shear gradient induced force. This is balanced by the wall repulsive force. Once the two forces are balanced, the particle has reached a region called equilibrium manifold, near the channel wall. At this point, the particle experiences a lateral migration towards the final focusing position. It is a slower

migration governed by the rotation of the particle. An empirical relationship for the lift coefficient was derived [18]:

$$C_L^+ \propto \frac{H^2}{a\sqrt{Re}} \tag{1.2}$$

Lift coefficients are associated with lift forces and the sign determines the direction of the force. In this case, the positive sign means that the rotation-induced force moves up to the velocity gradient, towards the lateral centerline of the channel, along the wall [18].

Among the weaker inertial forces there are:

1. The **Magnus** lift force, due to the pressure gradient around a rigid spherical particle, resulting from the asymmetry of the streamlines, generated from the rotation of the particle. In a microchannel this effect acts as a lift force directed upwards, and it was originally studied in the work by Rubinow and Keller [19]. This force is expressed as:

$$F_{RK} = \pi a^3 \rho \vec{\Omega} \times \vec{V} \tag{1.3}$$

where a is the radius of the spherical particle, ρ is the density of the fluid, $\vec{\Omega}$ is the angular velocity of the particle and $\vec{V}$ the velocity of the fluid. On the side where the spinning of the particle increases the velocity of the fluid, the pressure is reduced, thus the force is directed towards the high velocity region. A particle near a wall will migrate towards the center of the channel. This force is not dominant in the process of lateral migration of a spherical particle [20];

2. The **Saffman** force, or slip-shear force, is another inertial effect due to the presence of the walls. In this case, the effect is not related to the interaction of the particle with a single wall, like the wall-induced lift, but results from the particle lagging behind the fluid, which is indirectly caused by the presence of the channel walls. This results in a lateral force directed towards the center of the channel. If the particle is leading the flow instead of lagging, the force is directed away from the center of the channel. However, this force is only present in simple shear flows and not in Poiseuille flows, where most particles are more likely to undergo a shearing behavior. It is still important to mention this force, because it can play a major role in determining the final equilibrium position in specific cases, for example when the particle is not neutrally buoyant;

In curved channels, other phenomena can take place, such as the well-known **Dean flow**. It is a secondary flow appearing in curved channels or straight channels containing posts or other types of obstacles [21, 22]. Two symmetric vortexes are generated in the top and bottom part of the channel due to the difference in velocity between the region near the wall and in the center of the channel. The direct consequence is that a particle near the center will experience a centrifugal force directed outwards. The aforementioned vortexes are formed due to the re-circulation of the fluid near the wall.

1.2 Applications of inertial microfluidics

Inertial microfluidics can be applied to a variety of different fields and integrated into Lab-on-Chip devices, due to its portability and simplicity. In particular, its passive nature makes it extremely suitable for biological and medical applications [14]. These include cell cytometry,

enrichment, separation and sorting of cells and bacteria, also including blood cells, cancer cells, and budding yeast [13]. Flow cytometry is a basic analytical tool in biology, used to perform single-cell analysis. Conventionally, a train of cell passes through an optical detection system for analysis and counting. Inertial microfluidics has been successfully used to build different types of cytometry systems, reducing the cost, the amount of reagents required and the processing speed. [23]

In addition, the high-throughput of inertial microfluidics well integrates with high-speed imaging techniques. [24] The most common applications for this application are the identification of rare cells and cell phenotyping. [25] Other single-cell analysis applications include magnetic-inertial separation, PCR(polymerase chain reaction)-based detection, spectrophotometry and mass spectrometry. [23] In general, the most common targets are bacteria and circulating tumor cells (CTCs). [26–28] Cancer is characterized by the uncontrolled growth of malignant cells that can invade other districts of the body, resulting in metastases. During this process, cancer cells can be found in the blood stream, becoming CTCs. Therefore, they can be used as a fundamental diagnostic tool against cancer. However, CTCs are rare and difficult to isolate, but inertial microfluidics can help in their collection and counting.

Most of the works are developed in straight, curved and spiral channels, or a combination of them. Spiral channels are particularly suitable for separation and sorting, thanks to the presence of the secondary flows. Moreover, various cross-sections of the channel can be adopted, each of them with unique effects on the manipulation of the particles. The variety of possible combinations makes inertial microfluidics a versatile tool that can satisfy specific needs. In

the recent work published by Shiriny and Bayareh [29], they built a single loop spiral channel for the segregation of cancer cells from white blood cells (WBCs) and red blood cells (RBCs), achieving 100% of purity. The extraction of CTCs from a background population belongs to the more general field of **microfluidic-based cell separation**. The separation technology varies according to the channel geometry. [30] In straight channels, ones relies mainly on the lateral migration of the particles due to inertial forces. Common applications for straight rectangular channels involve the manipulation of bacteria, DNA, bubbles and droplets. [31–33] Arcuate channels have been used for the separation of polystyrene beads [34] and skeletal satellite cells for therapeutic purposes and tissue engineering. [35] Sinusoidal channels with various curvatures and serpentine channels have been used to separate polystyrene particles and to target cyanobacteria. [36] Spiral channels have been used for the manipulation of neutrally buoyant particles and cells [37], CTCs [38], micro-beads [39] and fluorescent beads. [40]

Finally, inertial microfluidics has been widely integrated with active microfluidics to improve the throughput, purity and efficiency of the separation. For example, it was combined with magnetophoresis and DLD for CTCs separation or with acoustic devices targeting fluorescent particles [41], bacteria in blood [42] and CTCs [43]. Also the dielectric technology was used for particle handling, such as in the work by Li *et al.* [44], where they built an integrated on-chip device for mRNA extraction in living cells.

In order to increase the efficiency and the purity of the process, different channel geometries and technologies can be combined in the so-called **multi-technology cascading channels**. When the chip is made only by different channel geometries connected in series or parallel, the

technique goes under the name of **single-technology cascading channel**. [30] For example, in Ren *et al.* 2021, serpentine channels were organized in parallel to scale up the throughput of separation of tumor cells. [45]

Overall, there is a huge amount of possible solutions depending on the specific application. Comprehensive design rules are still lacking, and providing a general framework is necessary, and also one of the aims of the present work. From the engineering perspective, beside the geometry of the channel, one can act on a set of parameters, some of which are described in the following section.

1.2.1 Parameters affecting inertial migration

In general, several parameters affect the final equilibrium position of a particle in a microchannel. These can be related to the channel topology, the fluid properties, flow conditions, particle characteristics or a combination of them. The flow rate affects the equilibrium position of a particle by shifting it closer to the wall when Re increases. In terms of forces, both the wall-induced and shear gradient-induced forces increase at higher Re, but the increment is higher for the latter. This have been previously observed by Segre and Silberberg [16] in circular ducts starting from $Re > 30$. Not only the flow conditions, but also the fluid properties can affect the final equilibrium positions. The rheological properties of non-Newtonian fluids introduce the viscoelastic force, that contributes to the lateral migration of a particle in a channel. Although the present study has been developed modelling a Newtonian fluid, like water, it is important to know that viscoelastic forces have been used for high-throughput separation and combined with inertial forces, also in computational studies [46]. An interesting way to manipulate particles

at the microscale is to exploit their own characteristics. Particle size determines the focusing position, which is shifted towards the nearest wall when the size is reduced. Bigger particles get closer to the center, due to the steric effect. Moreover, in real case scenarios, particles are not perfectly rigid, and especially bio-particles such as cells are deformable. Their deformability introduces a lift force perpendicular to the flow direction. The general trend is that softer particles focus closer to the channel center than stiffer particles. Another thing to take into account is the particle concentration. Higher numbers of particles can introduce a disturbance in the migration across adjacent streamlines, creating new focusing positions and affecting the particles spacing. Finally, particle shape affects the inertial migration process, in a way that still needs to be elucidated, and the current progress on the topic will be discussed next.

1.3 Inertial migration of shaped particles: state of the art

Spherical particles are relatively easy to investigate due to their symmetry and simplicity. Nonetheless, cells found in biological samples are best represented by deformable spherical particles, capable of changing their morphology. Therefore, shape and deformability could be used to distinguish between different cell types, cell states, and cell cycle stages [13], but also between eukaryotic cells and bacteria, that are generally non-spherical and approximately 10 times smaller [47]. Indeed, as it can be noticed from the previous list of applications, most of the studies on inertial migration have focused on spherical particles. There is a lack of experimental and computational studies on shaped particles due to the associated technical challenges. From the experimental side, non-spherical particles are difficult to manufacture, and from the computational side their complex dynamics make their simulations expensive and time consuming.

Common non-spherical particles include ellipsoids, such as prolate (λ = radial diameter/equatorial diameter > 1) and oblate ($\lambda < 1$), non-ellipsoids, such as rod-like and disk-shaped beads, and asymmetric particles.

The first theoretical study on ellipsoids was done by Jeffery in 1922 [1], considering a simple shear flow in Stokes regime ($Re = 0$). He showed that the particles rotate around their vorticity axis, which is perpendicular to the plane of the flow gradient, as shown in Figure 2a. He found that a particle can undergo a set of infinite possible orbits that depend on the starting orientation, the so-called Jeffery orbits, which include kayaking, tumbling, and log rolling (Figure 2b-d). He also studied the particle angular velocity and provided a formula to compute its orbit period given the aspect ratio and the shear rate. This mathematical framework was generalized for rigid bodies forty years later, in the work by F.P. Bretherton. [48] Even in this study, non-Newtonian and inertial effects were not considered. Bretherton also introduced the "mirror symmetry time reversal" theorem (MSTR theorem). In brief, it shows that if we consider a particle moving in a channel flow or a viscous shear flow, if we imagine to reverse time, we will obtain the mirror symmetric configuration in terms of flow, force and pressure field. The MSTR theorem is only valid if the particle is sufficiently symmetric. In a way, shaped particle may represent an exception to this theorem, thus they can be subjected to lift forces even if inertia is absent.

In the current literature, despite a significant number of studies of ellipsoidal particles in shear flows [49], there is little work on the rotational and inertial behavior of ellipsoidal particles in microchannels. For a non-spherical particle in a microfluidic system, lateral migration and

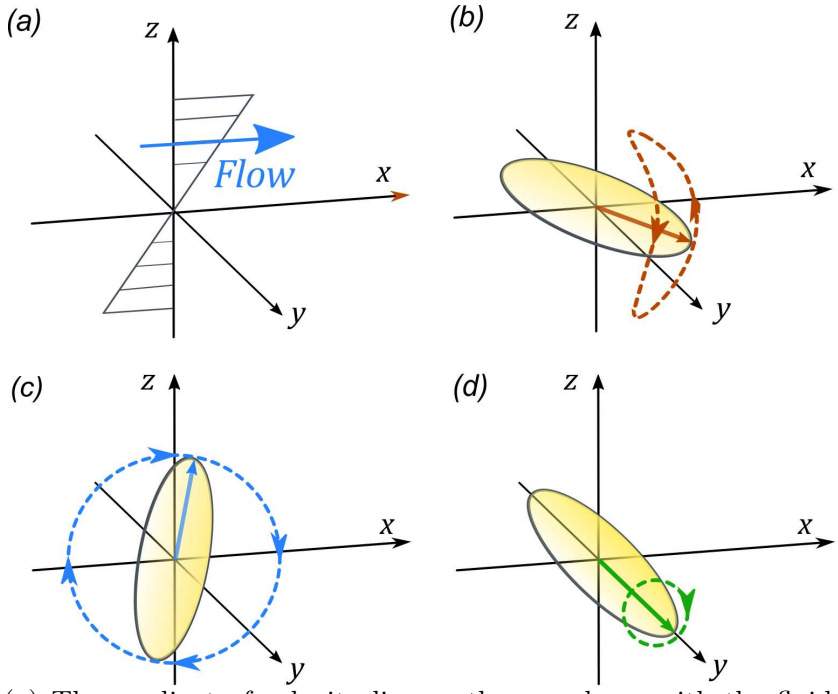

Figure 2: (a) The gradient of velocity lies on the x-z plane, with the fluid flowing in the x-direction. The vorticity axis, perpendicular to the flow-gradient plane corresponds to the y-axis. (b) Kayaking motion. (c) Tumbling motion. (d) Log-rolling motion.

the rotation are strongly related, and the experimental observation of exact motion is not trivial and requires new imaging techniques such as 3D reconstruction.

It has been shown that in a Poiseuille flow a prolate particle prefers to tumble [50,51], similar to the studies in shear flows. The main experimental work reported in literature on the study of the shape effects on the lateral migration and translational behavior is the one by Di Carlo and his coworkers [13,52]. Hur *et al.* [52] experimentally investigated the lateral and vertical equilibrium positions of a variety of artificial beads, with different size and cross-sectional shapes. From the numerical side, the complex rotational behavior of non-spherical particles is associated with a

smaller time step and requires a higher computational cost [53]. Lashgari *et al.* [2] mapped the inertial migration dynamics of oblate particles in square and rectangular microchannels. To the best of our knowledge, it is the only systematic computational investigation for ellipsoidal particles in a microchannel, but it was limited to oblate particles.

Prolate particles have been investigated even less than oblate particles. The only integrated experimental and computational study of prolate ellipsoids in a microchannel was performed by Masaeli *et al.* [13], who used prolate particles of different aspect ratios and compared experimental results with lattice Boltzmann and finite element simulations. They experimentally and computationally studied the shape-based separation of prolate ellipsoid, and applied the results to the enrichment of artificial beads and yeast. In this work, they distinguished between an in-plane rotation, when the particle rotates around the y-axis, and out-of-plane rotation, when there is any other component of rotation. Increasing the particle Reynolds number from 0.3 to 0.75, the percentage of in-plane rotations increases, and the rotational behavior is tumbling. The particle Reynolds number is defined as

$$Re_P = Re\left(\frac{a}{W}\right)^2 \tag{1.4}$$

where Re is the channel Reynolds number introduced in (Equation 1.1), while a and W are the diameters of the particle and the channel, respectively.

They have also compared the period of rotation from their simulations to the theoretical value from Jeffery's theory, mainly observing no significant variation and, concluding that inertia has

no notable effect on it. However, inertia reduced the infinite number of Jeffery's orbits to just one stable orbit, implying that the starting orientation does not influence the final equilibrium orbit. They observed how the rotation of the particles is responsible for the shape-dependent separation. Higher aspect ratio prolates focuses closer to the center of the channel since the repulsive wall lift from the wall is stronger, when the major axis of the particle is aligned perpendicular to the flow during the rotation. Finally, similar to what was reported by Hur *et al* [52], they confirmed that spherical and prolate particles with equivalent diameters have similar final equilibrium positions, and that the maximum rotational diameter is the main parameter responsible for the focusing positions.Yet, since these studies focused on experiments and applications [13, 52], a limited range of confinement ratios were investigated computationally. More important, the transient migration dynamics was less explored than the final focusing positions in these studies.

1.4 Overview of numerical analysis and mathematical modelling

In order to describe a physical problem, a suitable mathematical formulation is required. The general laws need to be particularized in the specific forces acting on a body. The equations constitute the basic relations within the model. In addition, a set of initial and boundary conditions must be considered. Once the model has been defined, the solution, in principle unique, should be found. The theoretical understanding of the existence and the smoothness of the solutions of the Navier-Stokes equation is still debated in the literature. The complexity of physical phenomena does not allow to find an exact solution to a given problem, most of the

time. For this reason, this needs to be approximated by a method, implemented on a computer, hence the definition of numerical methods. In this section, only a brief introduction is provided, following the treatment in ref. [54] After that, the mathematical model must be validated. This is a crucial step, to make sure that what the model produces is consistent with the results observed in the real case scenario. That is because a model is inherently prone to errors. This concept will be briefly mentioned next.

Numerical methods are an instrument that can be used to model reality and support experiments. Most of the real case problems do not have an exact solution, or we may need to capture some parameters that are not accessible *via* traditional experimental investigation. To do this, several mathematical instruments need to be combined to solve a set of governing equations. These include interpolation, numerical differentiation, numerical integration. There are several numerical methods to conduct simulations, which need to be suitable to the specific application. Regardless of the method, the common feature of numerical schemes is the discretization. It is a necessary step to make a continuum domain discrete. Space can be simplified with a grid or mesh, and time can be discretized with time steps. As previously mentioned, when doing this approximations, errors are inevitable. Here is a brief overview of the different types of errors that characterize numerical schemes:

1. **Round-off** error is related to the precision of the computer itself (*e.g.* single or double precision) and it is always present;

2. **Truncation** error: associated with the approximation of a mathematical procedure, *e.g.* approximating the derivative with finite differences. Using the Taylor expansion of $f(x)$, it is obtained that:

$$f'(x_0) = \frac{f(x_0+h) - f(x_0)}{h} - \frac{1}{2}f''(x_0)h - \frac{1}{6}f'''(x_0)h^2 + \dots \tag{1.5}$$

   where the first part is the the approximation of the derivative of f and the second part is the truncation error. It could be possible to choose more precise approximations, thus reducing the order of the truncation error;

3. The **Local truncation** error is the one introduced by a single step of the integration algorithm assuming that the previous step is the exact value of the function;

4. The **Global truncation** error is caused by the accumulation of the truncation error.

Besides the errors, numerical methods are characterized by fundamental properties, that should be taken into account when studying a numerical scheme or when trying to design a new one. Here are introduced some of these key concepts for numerical analysis:

1. **Stability**: it is assumed that the solution of the numerical problem is bounded. A method can be stable or unstable, and stability does not imply accuracy. In particular a method can be:

   (a) Unconditionally stable: the method is always stable (for any time step);

   (b) Unstable: the method is always unstable (for any time step);

(c) Conditionally stable: the method is stable only for some time steps or under a range of conditions;

2. **Accuracy**: it is the order of the truncation error, which can be amplitude errors or phase errors (if the phase is negative, it means that the solution is slightly behind the true value);
3. **Stiffness**: an integration problem whenever the ratio between the maximum and minimum eigenvalues is too large:

$$\frac{\lambda_{max}}{\lambda_{min}} \gg 1 \tag{1.6}$$

The choice of the time step size may depend from this property;

4. **Consistency**: a numerical scheme is consistent when, in the limit of the grid size, it goes to zero;
5. **Convergence**: the sequence arising from successive solutions (as the grid size goes to zero) approaches a limit.

The **Lax-Richtmyer** [55] theorem states that given a consistent numerical approximation of a problem, the stability is the necessary and sufficient condition for the numerical solution to converge to the analytical solution.

1.4.1 Outline of numerical differentiation and integration

Differential equations are useful to describe a variety of physical phenomena, for example in fluid dynamics with the Navier-Stokes equations. In this section, an outline of the main numerical techniques to solve differential equations and to tackle numerical integration are presented.

There are two main types of differential equations: **Ordinary Differential Equations (ODE)** and **Partial Differential Equations (PDE)**. An example for ODE is the equation governing the vibration of a mass connected with a spring and a damper, while Navier-Stokes equations are a set of PDEs, that will be briefly described later on. Typically there are three types of problems that can be solved. The initial value problems (IVPs), when the initial conditions are know, and the evolution of the phenomenon is the object of interest. For example, a system of particles with given initial coordinates and velocities, whose evolution dynamics is computed over time can be considered an IVP, commonly referred to as molecular dynamics. Secondly, the boundary value problems (BVPs), when the boundary values are provided, and the behavior of the function between them is to be determined. At the boundaries there can be distinguished essential boundary conditions or natural boundary conditions. In fluid mechanics, the essential boundary condition is typically the velocity, while the natural boundary condition is the stress. The third problem is the eigenvalue problem, namely when a linear operation is applied to a vector, and the result is a scalar (the eigenvalue) multiplying the vector itself. There can be also combined initial and boundary value problems.

ODEs and PDEs are characterized by an order, according to the maximum derivative present within the equation. In general, they can be mainly classified as linear versus non-linear differential equations, and homogeneous versus in-homogeneous differential equations.

1.4.2 First order ODEs and the model problem

In the design of numerical algorithms, it is useful to compare them with a model problem, to gain information related to their performance and stability. A simple **model problem** that can be used as an example is the following initial value problem defined as:

$$\frac{\mathrm{d}y}{\mathrm{d}t} = \lambda y, \quad y(0) = y_0 \quad \text{where} \quad \lambda = \lambda_R + i\lambda_I \quad \text{and} \quad \lambda_R \leq 0 \tag{1.7}$$

where λ is the eigenvalue of the problem, and in general it is a complex number. The nature of λ is associated to the nature of the analytical solution

$$y = y_0\, e^{\lambda t} \tag{1.8}$$

and λ has to satisfy some characteristics to guarantee consistency, convergence and stability. The goal is to extend the model problem to general non-solvable cases, investigating the stability, accuracy, and robustness.

In general:

$$e^{ix} = \cos x + i \sin x = e^{(\lambda_R + i\lambda_I)t} = e^{\lambda_R}\, e^{i\lambda_I t} = e^{\lambda_R}(\cos \lambda_R t + i \sin \lambda_I t) \tag{1.9}$$

and since the second part is bounded between 1 and -1, it follows that λ_R must be < 0.

At this point, the continuous function is discretized in a finite number of points. It is now

considered the model problem of the so-called difference equation, which is solved recursively as:

$$y_{n+1} = \sigma y_n \tag{1.10}$$

$$y_1 = \sigma y_0 \tag{1.11}$$

$$y_2 = \sigma y_1 = \sigma^2 y_0 \tag{1.12}$$

$$y_3 = \sigma y_2 = \sigma^3 y_0 \tag{1.13}$$

$$y_n = \sigma^n y_0 \tag{1.14}$$

and the solution is bounded for $|\sigma| \leq 1$.

The analytic solution is valid anytime. Assuming a constant time step Δt:

$$y_n = y_0\, e^{\lambda t_n} = y_0\, e^{\lambda \Delta t_n} \quad (\textbf{Differential} \text{ problem}) \tag{1.15}$$

$$y_n = \sigma^n y_0 \qquad\qquad (\textbf{Difference} \text{ problem}) \tag{1.16}$$

The equivalence between these 2 equations is:

$$\sigma^n = e^{\lambda \Delta t n} \quad \rightarrow \boxed{\sigma = e^{\lambda \Delta t}} \tag{1.17}$$

and in order to have stability, namely a bounded solution, the condition that must be satisfied is $|\sigma| < 1$, thus $e^{\lambda \Delta t} < 1$. The only way to satisfy this condition is to have the exponential decreasing:

$$\mathrm{Re}(\lambda \Delta t) = \lambda_R \Delta t < 0 \quad \rightarrow \quad \lambda_R < 0 \tag{1.18}$$

1.4.3 Integration schemes

When doing differentiation, it is generally possible to find the analytical solution. The same is not always true for integrals, for which numerical methods are particularly useful in practice. [56] Here are reported the main integration schemes, that can be useful to the reader to understand some part of the present work. Given a generic bounded differential equation

$$\frac{\mathrm{d}y}{\mathrm{d}t} = f(t, y), \quad t > t_0 \ \text{ and } y(t_0) = y_0 \tag{1.19}$$

the integration between two arbitrary time steps is:

$$\int_{t_n}^{t_{n+1}} \frac{\mathrm{d}y}{\mathrm{d}t} = \int_{t_n}^{t_{n+1}} f(t, y)\mathrm{d}t \tag{1.20}$$

$$y(t_n + 1) = y(t_n) + \int_{t_n}^{t_{n+1}} f(t, y)\mathrm{d}t \tag{1.21}$$

The integral, namely the area under the curve, can be approximated in a number of ways. These include rectangle methods, such as explicit and implicit Euler, and trapezoidal methods, such as the Crank-Nicolson scheme:

1. **Explicit Euler**

$$\int_{t_n}^{t_{n+1}} f(t,y)\mathrm{d}t \simeq f(y_n,t_n)\Delta t \tag{1.22}$$

2. **Implicit Euler**

$$\int_{t_n}^{t_{n+1}} f(t,y)\mathrm{d}t \simeq f(y_{n+1},t_{n+1})\Delta t \tag{1.23}$$

3. **Crank–Nicolson**

$$\int_{t_n}^{t_{n+1}} f(t,y)\mathrm{d}t \simeq \frac{f(y_{n+1},t_{n+1})+f(y_n,t_n)}{2}\Delta t \tag{1.24}$$

In the explicit methods, the solution at n+1 depends only on the previous step, whereas in the implicit ones we have a dependence on n+1 itself. Both Euler schemes have a first order accuracy (order Δt), and both schemes are also consistent: as Δt approaches zero, the solution approaches the true one. On the other hand, the Crank-Nicolson approach has a second order accuracy (Δt^2) and it is always stable. Since providing details on numerical analysis is out of the scope of this work, the reader is referred to textbooks, such as [56], for further information. In the next section, more details are provided on the numerical modelling of fluid dynamics.

1.5 CFD: numerical modelling of inertial microfluidics

Despite the great amount of experimental work published in the literature, since the discovery of inertial microfluidics by Segre and Silberberg, little work has been conducted to gain

more insights on the fundamentals of the phenomenon. Part of the underlying physics is still unknown and a lot of cases have not been investigated yet. Numerical simulations can be used to bridge this gap. The current application of computational fluid dynamics (CFD) on inertial microfluidics can be grouped into mesh-based and mesh-free methods. Numerical solutions can be further divided into Navier-Stokes-based solutions and Lattice Boltzmann Method (LBM). The asymptotic solutions were among the first to be adopted to predict the inertial behavior of a particle inside a channel and allowed to lay the fundamental principles of inertial microfluidics, following 1961. For example, asymptotic analysis is the method adopted in the previously mentioned work by Rubinow *et al.* [19] on the transverse force on a spinning sphere (1961) and the work by Saffman [57] on the lift force on a particle in shear flow (1965). These methods are able to provide an explicit formula of the force that is being studied, but they are limited. For complicated scenarios, the Navier-Stokes methods are more suitable. In general, the incompressible Navier-Stokes equations are probably the most important partial differential equations in fluid mechanics and they describe the motion of a Newtonian fluid.

$$\nabla \cdot u = 0 \tag{1.25a}$$

$$\rho \left(\frac{\partial u}{\partial t} + u \cdot \nabla u \right) = -\nabla p + \mu \nabla^2 u \tag{1.25b}$$

(Equation 1.25a) ensures that mass in conserved, since the divergence of the velocity field u is zero across the fluid. (Equation 1.25b) comes from Newton's second law, normalized by the infinitesimal volume of fluid which is being considered. In this case, ρ is the density of the

fluid, p is the pressure and μ is viscosity, that appears in the friction term. The Navier-Stokes equations assume that the fluid is a continuum, it is incompressible and isothermal [58]

1.5.1 Navier-Stokes-based numerical methods

As previously mentioned, the solutions coming from asymptotic methods are limited by the relatively narrow range of particle size and flow conditions that can be explored. Direct numerical simulations (DNS) are preferred for this purpose [53]. In this case, the fluid-particle interaction is considered for the computation of the inertial forces. Here is a list of the most common methods employed for a particle flowing in a channel:

1. **Flow at Specific Particle Position (FSPP)** is a method that computes the steady-state flow field around a particle, varying its position within the channel. In this way, it is not necessary to compute the whole trajectory of the particle in order to derive the inertial forces. Once the particle position has been chosen, the boundary conditions are applied: a fully developed laminarity flow at the inlet and outlet of the channel, moving walls and no-slip boundary condition at the particle surface. The particle is initially at rest. Then, Navier-Stokes equations are used to compute the pressure and velocity field around the particle, while the linear and angular velocities are calculated using Newton's second law;

2. **Arbitrary Lagrangian-Eulerian (ALE) method** considers a suspension of rigid particles and solves the incompressible Navier-Stokes equations, typically using finite elements. The particle velocity, orientation and position are obtained *via* the integration of the total stress on the surface of each particle. However, this method has several limitations. If

the particles are not neutrally buoyant, the scheme might lead to an unstable solution. Moreover, the mesh needs to be updated at every time step, thus the method is extremely time-consuming;

3. **Fictitious Domain Methods** are similar to ALE methods, but a fixed mesh that covers the entire domain (particle and fluid) is used instead. The key point of this method is that, since the mesh spreads across the whole domain, a force needs to be applied to the particle grid points so that it behaves as a rigid body. This method may be referred to as immersed boundary method (IBM), when the force is applied to the surface of the particle, or immersed body method, if this force is applied to the body of the particle [53];

4. The **Immersed Boundary Method (IBM)** was first introduced by Peskin in 1972 [59], and allows to perform the simulation of the flow on a fixed grid [60]. At the same time, there is a second mesh that is distributed at the surface of the particle. These two meshes are typically called Eulerian and Lagrangian mesh, respectively. In general, the latter does not align with the former grid, and the computational cells are cut. Several variants of the IBM were developed after his first appearance, to accommodate the possible types of geometries in a flow and to treat the cut cells. [61] The Lagrangian mesh is constituted of elements Δv_l with markers X_l located at the center of each element. In the case of a particle flowing in a microchannel, the main goal is to compute the force distribution.

$$u(X_l, t) = \sum_{ijk} u_{ijk}(x_{ijk}, t)\delta_h(x_{ijk} - X_l)\Delta x \Delta y \Delta z \tag{1.26}$$

This is done by interpolating the value of velocity of the Eulerian grid with the Lagrangian markers, following (Equation 1.26). In the second place, the difference between the interpolated velocities and the particle velocity gives the forces acting on the Lagrangian mesh:

$$f(x_{ijk}, t) = \sum_{l} \rho \frac{U_p(X_l, t) - u(X_l, t)}{\Delta t} \delta_h(x_{ijk} - X_l) \Delta v_l \tag{1.27}$$

In both (Equation 1.26) and (Equation 1.27), $\delta_h(x_{ijk} - X_l)$ is the Dirac delta function used to interpolate the two meshes. The last step is to add the force term computed from (Equation 1.27) to the Navier-Stokes equation, in order to finally derive the motion of the particle. The way the boundary is treated leads to different variants of the methods. For example, Lashgari and his coworkers [2] used IBM to describe the inertial migration of oblate particles in straight ducts, using the discrete forcing method to compute the fluid-solid interaction. This variant was first introduced by Uhlmann in 2005 [62] and modified by Breugem in 2012 [63] for neutrally buoyant particles.

Overall, the generation of the grid is easy in IBM, but it is limited by the complicated implementation of the boundary conditions. [64]

1.5.2 Lattice Boltzmann Method (LBM)

CFD generally refers to the direct discretization of the governing partial differential equations (PDEs), such as the Navier-Stokes equations. LBM has emerged as an alternative approach to CFD, and it was originally introduced by McNamara and Zanetti in 1988 [65], originated from its earliest form of *Lattice gas automata* (LGA). [66]

The basic concept of LBM is to solve the kinetic equation for the particle distribution function. [67] The general idea is to derive information of the macroscopic behavior of the fluid from its microscopic properties, such as the density. At the microscale, density and velocity needs to be redefined. The velocity vector can point in any direction, and this leads to a zero velocity at the macro scale. However, the average velocity magnitude is not zero, and from this, one can derive the mean kinetic energy. Overall, a certain probability of finding a particle with a given velocity magnitude is introduced. The distribution of velocities is dependent on the temperature. When describing particles, the information of their position and speed is integrated. That is why a distribution function is introduced. The particles are described with a propagation and collision step over a discrete lattice. The classic Boltzmann equation for a single particle can be written as:

$$\frac{\partial f}{\partial t} + c \cdot \frac{\partial f}{\partial r} + F \cdot \frac{\partial f}{\partial c} = Q(f) \tag{1.28}$$

where c is the particle velocity, F is the body force and $Q(t)$ is the collision term. A common linearized form of the collision term is widely employed nowadays and it is described by the Bhatnagar–Gross–Krook (LBGK) collision model. [68] (Equation 1.28) is than discretized in space and time. The resulting LBM equations consider a population of particles at a given position and time, and the one at the following time step, that will have moved according to the velocity of the considered population. This is set equal to the collision operator, according

to the adopted formulation.

For example, for the LBGK single-relaxation-time model we have:

$$f_i(x + c_i\Delta t, t + \Delta t) - f_i(x, t) = -\frac{1}{\tau}\left(f_i(x, t) - f_i^{(0)}(x, t)\right) \tag{1.29}$$

where $f_i(x,t)$ and $f_i^{(0)}(x,t)$ are the particle and equilibrium distribution functions at a given position and time, c_i is the particle velocity along the i^{th} direction considered, and τ is the single-relaxation-time parameter, which is responsible for the rate at which the equilibrium is approached. (Equation 1.29) [69] is then divided into a collision and streaming step.

The key differences between Navier-Stokes based methods and LBM are [67] the nature of the equations adopted, the linearity of convection terms and the continuum assumption, which is not present in LBM. For more information and a complete description of the methodology of LBM, please refer to textbooks [70] and [71].

1.5.3 From mesh-based to mesh-free methods

All the numerical schemes solving fluid dynamics problems described so far are mesh-based methods. It means that they either use a Lagrangian mesh or Eulerian grid to create a relationship between nodes, which are the constitutive blocks of the numerical scheme. Recently, it has become clear that many of the academic researches and industrial applications cannot be easily solved with conventional mesh-based methods, especially when large deformations are involved, such as in fluid mechanics. [72] In the presence of discontinuities, the common solution to preserve the grid is to re-mesh the domain, and this increases the computational cost and reduces

the accuracy of the solution. The purpose of mesh-free methods is to overcome the drawbacks of mesh-based methods, thus to broaden the range of possible applications. However, in some cases traditional methods are still more convenient, and a lot of research is going on to better understand the performance of these techniques. [73] Mesh-free methods use a set of nodes to represent the entire domain and boundaries, and these nodes are used to locally approximate the field variables. [74]

The basic steps to build a mesh-free method are:

1. **Domain representation**: the domain is represented with a distribution of nodes, also called *field nodes*, and the boundary conditions are applied. The nodal density can be uniform or adapted depending on the specific applications;
2. **Interpolation**: a support domain is used to interpolate the field variable of interest. The support domain describe a geometric region with center $\mathbf{x}$, that contains the nodes, now called *support nodes*, that will be used to approximate the field variable at the point $\mathbf{x}$. The support domain can have different shapes and a weighting function is used to compute the average field variable from all the support nodes;
3. **Building the system equations**: this step changes accordingly to the specific method. The global system equations can be a set of algebraic, eigenvalue or differential equations depending on the type of problem;
4. **Solving mesh-free equations**: the solving techniques depend on the nature of problem. For dynamic problems, one wants to obtain the history of the displacement, velocity,

and acceleration, and this can be done with finite difference methods, either implicit or explicit. [74]

The key feature of mesh-free methods is the creation of the shape function. Ideally, it should satisfy several requirements, that are listed in [74]. Some of them are herein reported:

1. First, the shape function should satisfy the Delta function property and defined accordingly. The Kronecker delta is defined as:

$$\Phi_i(x_j) = \begin{cases} 1 & \text{when } i = j \\ 0 & \text{when } i \neq j \end{cases} ; \tag{1.30}$$

2. The support domain of the shape function should be compact, meaning that it should contain a small number of nodes;
3. The nodal distribution should be arbitrary;
4. The algorithm should be efficient and stable.

The different ways to construct a shape function can be grouped in: integral representation method, series representation method, differential representation method and gradient smoothing method.

The earliest mesh-free method to be developed was smoothed particle hydrodynamics (SPH), described by Lucy, Gingold and Monaghan [75, 76] in 1977. Following this, the diffuse element method (DEM) was proposed in 1992, the element free Galerkin (EFG) method in 1994, based on DEM, point interpolation method (PIM) in 1999, mesh-free weak-strong form (MWS) in

2002 and many others. [77]

In the present work, we used SPH to model a multi-phase flow in a inertial microfluidic configurations. The next section is devoted to the description of the numerical method and its implementation.

CHAPTER 2

METHODOLOGY

Reproduced from [Lauricella, Giuseppe, et al. "Computational study of inertial migration of prolate particles in a straight rectangular channel." Physics of Fluids 34.8 (2022): 082021], with the permission of AIP Publishing

2.1 Smoothed Particles Hydrodynamics (SPH)

SPH is a mesh-free Lagrangian method, originally designed for astrophysical problems [75], but it is also widely employed for various fluid mechanics problems [78]. It has several advantages over traditional finite difference methods, such as a straightforward handling of the interface between different materials, and the fact that the computations take place only where there are material particles. [79] In the classical SPH approach, a state equation for a weakly compressible fluid is used to approximate the incompressibility of the Navier-Stokes equations [76]. The general idea of SPH is to represent the fluid domain with Lagrangian particles, *i.e.* SPH particles. Each of these particles has its own mass, velocity, energy, and other properties. Navier-Stokes equations are discretized using SPH particles and a set of field variables, such as density and velocity, are interpolated by means of a kernel function, which decays to zero within a range of the smoothing length h. From the mathematical point of view, SPH particles can be seen as interpolation points to compute the fluid properties, and their interaction reproduces the governing equations. [79]

In the original proposed version of SPH, the conservation of linear and angular momentum was not ensured. The model was improved in 1982 [80], when the similarities with molecular dynamics became more obvious, later explored more in detail by Hoover and coworkers. [81,82] SPH is preferable over traditional mesh-based methods when large perturbations are involved. [79] Although SPH has been applied and validated for many fluid mechanics applications, it has not been widely used for inertial microfluidics simulations. The group led by Peng and Papautsky successfully applied SPH to study the transient motion of rigid spheres in straight rectangular channels. [83] The computational predictions match well with the high speed fluorescence imaging trajectories, demonstrating that SPH is a reliable modeling approach in predicting the trajectory and equilibrium position of spherical particles in inertial microfluidics.

2.1.1 Interpolation

In general, fluid dynamics equations have the form

$$\frac{\mathrm{d}A}{\mathrm{d}t} = f(A, \nabla A, r) \tag{2.1a}$$

$$\frac{\mathrm{d}}{\mathrm{d}t} = \frac{\partial}{\partial t} + v \cdot \nabla \tag{2.1b}$$

where (Equation 2.1b) defines the Lagrangian derivative and the differential operator represents the trajectory of a fluid particle. [79]

The integral interpolant for an SPH quantity A is:

$$A_I(r) = \int A_I(r')W(r - r', h)\mathrm{d}r' \tag{2.2}$$

where W is a kernel function, that approximates the Dirac delta function, and $\mathrm{d}r'$ is an infinitesimal volume element. [79] This integral can be approximated by doing a summation over the mass elements.

For each field variable A, the local average at position r_i is computed as:

$$A\left(r_i\right) = \sum_j m_j \frac{A_j}{\rho_j} W\left(r_i - r_j\right), \tag{2.3}$$

where m_j and ρ_j are the value of mass and the density of the particle at position r_j. One possible kernel, proposed originally by Lucy, is a bell-shape kernel function [75]. Other popular kernel functions include the Gaussian, cubic spline and B-spline, fourth and fifth spline [84]. The estimation of the error for the integral interpolant is difficult due to the disordered motion of the Lagrangian particles, thus it is highly dependent on the dynamics of the system.

2.1.2 SPH acceleration equation

The SPH version of computing the acceleration was presented in the original work of 1977 by Lucy, Gingold and Monaghan [75, 76] as:

$$\frac{\mathrm{d}v_i}{\mathrm{d}t} = -\frac{1}{\rho_i} \sum_j m_j \frac{P_j}{\rho_j} \nabla_a W_{ij} \tag{2.4}$$

where the subscripts i and j refer to the Lagrangian particle considered.

$$\frac{m_i m_j P_j}{\rho_i \rho_j} \nabla_i W_{ij} \neq \frac{m_i m_j P_i}{\rho_i \rho_j} \nabla_j W_{ij} \tag{2.5}$$

As anticipated before, in this original formulation the conservation of momentum is not exact, meaning that the force that a particle j exerts on a particle i in not opposite and equal to the force on the particle i owing to j, as shown in (Equation 2.5). The problem was solved using a Lagrangian. [80]

2.1.3 Lagrangian equation in SPH

Considering the motion of a fluid in a potential $\Phi(r)$ with no dissipation, the Lagrangian L is [85]:

$$L = \int \rho \left(\frac{1}{2} v^2 - u(\rho, s) - \Phi \right) \mathrm{d}r \tag{2.6}$$

where u is the specific thermal energy, ρ the density and s is the entropy.

The corresponding SPH version of (Equation 2.6) is:

$$L = \sum_j m_j \left(\frac{1}{2} v_j^2 - u(\rho_j, s_j) - \Phi_j \right) \tag{2.7}$$

and for a particle i one finds that:

$$\frac{\mathrm{d}}{\mathrm{d}t} \left(\frac{\partial L}{\partial v_i} \right) - \frac{\partial L}{\partial r_i} = 0. \tag{2.8}$$

With the introduction of (Equation 2.8), it is possible to re-write (Equation 2.4) as:

$$\frac{\mathrm{d}v_i}{\mathrm{d}t} = -\sum_j m_j \left(\frac{\partial u}{\partial \rho} \right)_s \frac{\partial \rho_j}{\partial r_i} - \frac{\partial \Phi_i}{\partial r_i} \tag{2.9}$$

2.1.4 Momentum conservation

Thanks to the invariance of the Lagrangian (Equation 2.7), the fluid dynamics terms conserve their linear and angular momenta. [79] This is valid for the entire system. In a way, a SPH system behaves as a system of molecules exerting a force between them, but the strength of the interaction, modulated by P and ρ, depends on the position of the surrounding particles. [79] SPH interpolants are applied to the Navier-Stokes equations. The equations are split into the individual forces: these leads to the main formulation for momentum conservation:

$$\left(\frac{\mathrm{d}u}{\mathrm{d}t}\right)_i = -\sum_j m_j \left(\frac{P_i}{\rho_i^2} + \frac{P_j}{\rho_j^2}\right) \nabla W(x_{ij}, h) \tag{2.10a}$$

$$\left(\frac{\mathrm{d}u}{\mathrm{d}t}\right)_i = \sum_j m_j \frac{\mu_i + \mu_j}{\rho_i \rho_j} \frac{x_{ij} u_{ij}}{|x_{ij}|^2} \nabla W(x_{ij}, h) \tag{2.10b}$$

where (Equation 2.10a) is the formulation for the pressure force [86, 87], and (Equation 2.10b) represents the viscous force. [88] The resulting force on the particle i is given as

$$F_i = -\sum_j m_i m_j \left(\frac{P_i}{\rho_i^2} + \frac{P_j}{\rho_j^2}\right) \nabla_j W_{ij} + \sum_j \frac{m_i m_j (\mu_i + \mu_j)}{\rho_i \rho_j} \left(\frac{1}{r_{ij}} \frac{\partial W_{ij}}{\partial r_i}\right) \tag{2.11}$$

by combining (Equation 2.10a) and (Equation 2.10b). (Equation 2.11) is the final momentum equation for two interacting particles i and j. In (Equation 2.11) m is the mass, ρ is the density, P is the pressure tensor, W_{ij} is the kernel function, μ is the dynamic viscosity and r the position vector of the considered particle.

2.1.5 SPH formulations

In the history of SPH, two main families of formulations have been developed and widely employed: a 'weakly compressible' variant (WCSPH) [89] and a family of 'incompressible' SPH (ISPH). [6]

In WCSPH, a stiff equation is used to relate pressure and density in viscous isothermal fluids, using an explicit timestepping method. ISPH methods uses the pressure-correction idea of grid methods and it is a semi-implicit method. [90] In the latter case, the particle density does not change, and this ensures the incompressibility of the fluid. Generally, the pressure Poisson's equation (PPE) is solved

$$\nabla \left(\frac{\nabla P^{n+1}}{\rho} \right) = \frac{3}{2\Delta t} \nabla \cdot u \tag{2.12}$$

while in WCSPH an artificial equation of state is used, such as

$$P = c^2(\rho - \rho_0) \tag{2.13}$$

where c is the sound speed and ρ is the density.

In the case of intermediate density values, the standard projection method of ISPH can accumulate errors, therefore ISPH has been modified, sometimes resulting in an increased computational cost, such as calculating the PPE twice in a single timestep. [91] One important feature to consider in SPH simulations and in the comparison between different formulations is the Mach number and the speed of sound. The Mach number is used in fluid dynamics and it is the ratio of the local flow velocity with the sound speed in the fluid, therefore it is a dimension-

less number. It can be seen as a measure of the compressibility of a fluid flow. Different Mach regimes can be distinguished such as subsonic (<0.8), transonic (0.8 - 1.2), supersonic (1.2 - 5.0) and hypersonic (5.0 - 10). In general, WCSPH provides a more ordered particle distribution and ease of programming. [92] However, for flow high Reynolds number flows, where $Re > 100$, WCSPH presents wide density variations, thus the speed of sounds needs to be increased, using a much smaller Mach number, generally lower than 0.1. This impacts the computational cost, since increasing the sound speed implies a reduction of the time step, to avoid instabilities, and this affect the simulation time. Violeau and Leroy [93] investigated how the flow conditions, boundaries and time-integration affects the maximum time step allowed in weakly compressible SPH, finding that the general stability criterion of SPH

$$C^h = \frac{c_0 \Delta t}{h} \leq 0.4 \tag{2.14}$$

could be increased for practical problems.

2.2 Overview of parallel computing

All the equations and numerical schemes presented so far need to be computed a high number of times, in order to collect a sufficient number of data, over a given period of simulation time. Memory-intensive computations can be solved with greater speed using parallel programming. It relies on message passing libraries, that mediate the transfer of data within the parallel architecture.

Parallel computers can work with a shared memory, distributed memory or a combination of

them. A shared memory is made of multiple processors that can access a global shared memory *via* a memory bus. A distribute memory architecture can be seen as a set of serial computers, called **nodes**, that communicate each other by means of a communication network. [94] MPI (Message Passing Interface) is a standardized message-passing library for C, C++, and Fortran programs running on parallel architectures. A parallel computer can be seen as a combination of processors, memory modules and an interconnection network, which allows the communication between different CPUs and memory modules. The way these objects are connected determines the working style of the computer. [95] Briefly, following the architectures classification defined by Flynn, commonly known as Flynn's taxonomy [96], there can be distinguished four main categories:

1. Single instruction stream, single data stream (SISD), used by serial computers;
2. Single instruction stream, multiple data streams (SIMD), where calculations can be either executed sequentially or in parallel;
3. Multiple instruction streams, single data stream (MISD), used for uncommon architectures that operates on a single data stream and must agree each other;
4. Multiple instruction streams, multiple data stream (MIMD).

Numerical simulations have become an ubiquitous tool in scientific research, and the need of high performance computing (HPC) is essential. For more information on parallel computing, the reader is addressed to the textbooks [97, 98].

2.3 Fundamentals of molecular dynamics

In the present work, smoothed particle hydrodynamics was implemented in LAMMPS (Large-scale Atomic Molecular Massively Parallel Simulator) [99], a molecular dynamics code, that is also used for particle-based algorithms such as SPH. It was introduced in 1994 by Steve Plimpton (Sandia National Laboratories) [99] and its use has been increasing for a variety of applications. The current version of the code, released as open source in 2004, is written in C^{++}, which is suitable for high-level programming due to its object-oriented nature. Molecular dynamics (MD) has been widely used in physics, chemistry, biology and many more research fields. In this approach, Newton's equation of motion are integrated over a given number of time steps, to model the time evolution of a system of particles. [99] MD well suites the rapid development of CPUs and GPUs, together with parallel computing, that will be briefly described later on. LAMMPS is among a variety of parallel MD codes, such as NAMD [100], GROMACS [101], and CHARMM [102], and it has a focus on material modelling.

The way the code integrates with distributed memory parallel computers is by partitioning the simulation box. It is divided into uniform pieces, and each of them is assigned with an MPI rank (a processor). However, one important parameter to take into account during this process is the density within the simulation. If it's not uniform across the simulation domain, the parallelization becomes inefficient, since the entire simulation will be limited by the slowest processor, namely the one assigned with an high-density subdomain. In this case, the partitioning is controlled by a dynamic load-balancing algorithm, thus the subdomain distribution will not

be uniform, but it will accommodate the density gradient instead.

Each processor collects and manages two types of data:

1. The positions, velocities and other information of all the atoms in its subdomain, called owned atoms;
2. Information related to atoms belonging to nearby MPI ranks, within a certain cutoff threshold, called ghost atoms.

Another key concept is the neighbor list [103]. Among all the structures in LAMMPS, this is one of the most memory-consuming. The idea of this list is to perform the force computation efficiently for each atom i, considering only the neighboring atoms j in the list for that atom i. The cutoff distance is chosen by the user, as well as the number of time steps to be used to re-build the list. The cutoff distance is defined as:

$$R_n = R_f + \Delta s \tag{2.15}$$

where R_f is the short-range pairwise forces cutoff of the interatomic potential, while Δs is called skin distance. When any atom has moved half the skin distance, the re-neighboring is triggered. This is an important step, where atoms that have moved are re-assigned the correct processor and periodic boundary conditions are enforced. Moreover, to improve chace efficiency, from time to time every processor spatially reorder its owned atoms, to benefit the force computation and the building of the neighbor list. [99, 104]

An interatomic potential is a function approximating the electronic energy of a system. The

gradient of these functions determines the forces between atoms, needed in MD simulations. Interatomic potentials can be classified according to the number of bodies participating in the interaction, bonding topology and chemical nature. [105] One of the most used potential in MD is the Lennard-Jones potential [106], suitable for entities with species with closed-electrons shells, and it has the form:

$$U(r) = U_0 \left[\left(\frac{r_0}{r} \right)^{12} - 2 \left(\frac{r_0}{r} \right)^{6} \right] \tag{2.16}$$

where r_0 is the equilibrium bond length between the two species and U_0 is the binding energy. It is a two-body potential, with an attractive and repulsive term. The atoms get too close to each other, the energy increases rapidly. When the distance increases, the energy approaches zero.

In molecular dynamics, the forces are given in terms of an empirical potential, and the potential energy can be written as [107]:

$$\begin{aligned} E = & \sum_{\text{bonds}} \frac{a_i}{2}(l_i - l_{i0})^2 + \sum_{\text{angles}} \frac{b_i}{2}(\theta_i - \theta_{i0})^2 + \sum_{\text{torsion}} \frac{V_n}{2}(1 + \cos(n\omega - \gamma)) + \\ & + \frac{1}{2}\sum_{i=1}^{N}\sum_{j \neq i}^{N} 4\varepsilon_{ij} \left[\left(\frac{\sigma_{ij}}{r_{ij}} \right)^{12} - 2 \left(\frac{\sigma_{ij}}{r_{ij}} \right)^{6} \right] + \frac{1}{2}\sum_{i=1}^{N}\sum_{j \neq i}^{N} 4\frac{q_i q_j}{r_{ij}} \end{aligned} \tag{2.17}$$

In general, the energy is a contribution of bonded interactions, given by the first three terms in (Equation 2.17), and non-bonded interactions, given by the last two. The first term is an harmonic potential representing the internal bonds of a molecule, accounting for the energy when the bond length l_i deviates from the length at rest l_{i0}. The same concept applies for the second and third terms. The fourth term is a Lennard-Jones potential constituting the van der

Waals potential and the last term is the coulombic interaction.

In MD, the electrostatic interactions represent the most expensive part of the simulation and their computational handling can be problematic, for two main reasons:

1. The finite size of the simulation domain and the mathematical discretization cannot deal with the in principle infinite long-range interaction;
2. Even a limited calculation can be very expensive due to the general high number of atoms/particle within a numerical simulation. [107]

Within LAMMPS, the long-range interaction of charged systems using a variety of methods, such as the FFT-based particle-particle/particle-mesh method [108, 109], particle-mesh Ewald (PME) method [110], or the multilevel summation method (MSM). [111]

2.3.1 Thermostatting and Barostatting

Another fundamental aspect of molecular dynamics is controlling the conditions of the system throughout the simulation. Thermostatting is the process of controlling the temperatures of the particles in a simulation, by means of a "thermostat". A similar concept can be extended to a simulation at a constant pressure, controlled by a "barostat". In general, a system can be defined as a statistical ensemble, that can be considered as a simplified version of the more complex real scenario, where multiple states co-exist. A system which is completely isolated from the surrounding is called microcanonical ensemble (NVE), which is defined in terms of the number of particles in the system (N), its volume (V) and its energy (E), which are all constant. If we allow the system to change its energy, we have a canonical ensemble. In this

case, the system is in contact with an heat bath, the thermostat, which allows to set a constant temperature. If also the pressure is set to be constant, the ensemble is called isothermal-isobaric, often abbreviated with NPT. Some thermostats and barostats that are commonly used in MD are the Nose-Hoover, the Andersen and the Berendsen thermostats and barostats.

2.4 The LAMMPS code

Starting from its original version in Fortran, LAMMPS was designed to be compatible with MPI. Within LAMMPS, it is possible to defined a 2D or 3D simulation box, whose boundaries can be fixed, which means that if a particle moves outside the box it is deleted, or they can be periodic, that is when a particle exits from one side of the box it will re-enter from the other side. Finally, the faces of the box can also be shrink-wrapped, meaning that the box can change in size to always enclose all the atoms or particles inside itself. [99] One of the key features of LAMMPS is its **flexibility**, so that the user can accommodate his specific needs. This can be done by acting on the input script, by the modification of the source code and by using LAMMPS as an external library. [99] In this section, only the first two methods will be described.

The input script of LAMMPS is a text file, where commands are invoked to build the simulation environment and the dynamic of the system. Each command has its own arguments and syntax rules that must be followed, to guarantee the correct execution of the code. In the script, variables can be defined, read or computed from a mathematical expression, which can also contain outputs from the simulation itself. [99] The main source of flexibility is represented by the variety of commands that can act on different atoms and produce different types of outputs,

that can be related to specific groups of atoms and processors. In LAMMPS it is possible to define static or dynamic *groups* of atoms, which the user can operate on. The outputs can be *per-atom* quantities, internally stored by the MPI rank owning the atom, or *global* properties, for which each processor possesses a copy. *Per-atom* properties confer a lot of flexibility, since the user can assign them to groups or chunks of atom, providing different behaviors. One can customize the entire simulation including the simulation box, the atom type, interatomic potentials, boundaries, groups of atoms, neighbor lists, data handling (space and time averaging is also possible), definition of variables, property definition and output post-processing. [99]

The second way to modify LAMMPS is to act on the C^{++} source code, especially at its high-level. The main functionalities of LAMMPS are organized into classes. [99] There can be distinguished core classes and parent classes, called *styles*. The user can add child classes by modifying the parent class, including a few methods and adding it to the source folder. [99] This structure favors modularity and sets of child classes related to specific applications are grouped into *packages*, and the users can choose which of them include in their LAMMPS build. [99]

2.4.1 Atom styles

Per-atom properties are defined by atom styles. These can be extremely different considering the variety of models that can be implemented. For example, for dynamic-size electron particles one needs to store their radius and radial velocity, or internal energy and heat capacity for SPH particles and dissipative particle dynamics (DPD). With the `atom_style` command in the LAMMPS input script it is possible to determine the attributes assigned to the atoms in a simulation. [99,112] If a style belongs to a package, it will not work if the packages was not build.

Some styles include: *atomic* (liquids, solid, metals), *ellipsoid* (aspherical particles), *molecular* (uncharged molecules), *charge* (atomic system with charges), *full* (a combination of *molecular* and *charge* styles, suitable for bio-molecules), *sph* (for SPH particles). LAMMPS also allows to generate hybrid styles, concatenating multiple atomic properties to obtain more complex models, for example adding charges to SPH or DPD particles.

2.4.2 Pair styles

These classes allow the implementation of pairwise interatomic interactions, following the general structure of (Equation 2.17). LAMMPS include more than 230 pair styles, including many-body potentials such as AIREBO [113], embedded atom method (EAM) [114] and many more. In addition to all-atom simulations, in order to achieve longer space and time scales it is possible to implement coarse-grained models. These were developed for polymers [115,116] and other systems, most of them with specific LAMMPS packages. The most related models to the present work are particle-based models.

Pair styles work with a *compute()* method, which is invoked every time step to compute the forces on each atom. Similarly to the atom style, it is possible to combine multiple pair styles in the same model using the *hybrid* pair style. [99] Once the most appropriate pair style has been selected, the `pair_coeff` command is used to specify the pairwise coefficients of the force field. A comprehensive updated list of all the pair styles available in LAMMPS can be found in the online **LAMMPS documentation** (docs.lammps.org/Manual).

2.4.3 Fix styles

During a time step, *fix* commands allow to implement specific operations. One fix style can use multiple methods, that are invoked in different moments of each time step. Commonly, fixes act on atom groups and they can be invoked multiple times. For example, in the present work, in order to define the suspended ellipsoidal particle in the flow, the *fix rigid* command has been applied to a group of atoms, to distinguish them from the background fluid particles. In general, a fix can be applied during timestepping or minimization. In LAMMPS there are hundreds of fixes, that allow the control over forces, temperature, boundaries and many more. Some examples include *fix addforce*, to add a force to a group of atoms, *fix ave_ chunk*, to compute per-chunk time-averaged quantities, *fix ave/time*, to compute/output global time-averaged quantities, *fix move*, to move atoms in a desired way, or *fix rigid/meso*, constrain clusters of SPH or DPD particles to behave as a rigid body.

A comprehensive list of all the fix styles available in LAMMPS can be found in the online **LAMMPS documentation** (docs.lammps.org/Manual).

2.5 Implementation of SPH in LAMMPS

The USER-SPH package was introduced by Georg Ganzenmuller in 2011. In this section, a summary of the relevant information present in the user guide [117] is given. The package introduces four new per-particle variables: the internal energy E, the local density ρ, and their derivatives $\dot{E}$ and $\dot{\rho}$. These new information are collected in a new data structure and accessible

using `atom_style meso`.

The local density is computed using Equation (Equation 2.3) as:

$$\rho_i = \sum_j m_j \frac{\rho_j}{\rho_j} W_{ij} = \sum_j m_j W_{ij} \tag{2.18}$$

and it is a smoothed quantity resulting from the contribution of the particle of the support domain. In LAMMPS, its calculation is invoked using

```
pair_style sph/rhosum
pair_coeff I J h
```

where `I` and `J` are the SPH particles considered for the calculation of the local density, and `h` is the radius of the kernel function, defined as

$$W(r < h) = \frac{1}{s}\left[1 - \left(\frac{1}{h}\right)^2\right]^4 \tag{2.19}$$

where s is a normalization constant. The local density can be also assigned at the beginning of the simulation using a `set` command.

2.5.1 Equation of State

The equation of state determines the pressure as a function of the temperature the ρ.

$$P(\rho) = \frac{c_0^2 \rho_0}{7}\left[\left(\frac{\rho}{\rho_0}\right)^7 - 1\right] \tag{2.20}$$

The Tait equation of state (EOS) (Equation 2.20) computes the pressure as a function of the local density and the temperature, where c_0 is the speed of sounds and ρ_0 is the density at zero applied stress. It is combined with (Equation 2.11), namely Morris expression [88] for laminar viscosity in our simulations. (Equation 2.20) is an incomplete EOS to model water at ambient conditions. It is selected in LAMMPS using:

```
pair_style sph/taitwater

pair_coeff I J rho_0 c_0 alpha h
```

where the `alpha` coefficient determines the strength of the artificial viscosity according to the equation:

$$\prod_{ij} = -\alpha h \frac{c_i + c_j}{\rho_i + \rho_j} \frac{v_{ij} \cdot r_{ij}}{r_{ij}^2 + \varepsilon h^2} \tag{2.21}$$

where c_i and c_j are the speed of sound of the particles and ε is a constant value which in this case is set such that $\varepsilon \simeq 0.01$.

Moreover, the `h` coefficient that appears in the `pair_coeff` command is the smoothing length of the Lucy kernel [75]:

$$W(r < h) = \frac{1}{s}\left[1 + 3\frac{r}{h}\right]\left[1 - \frac{r}{h}\right]^3 \tag{2.22}$$

The Tait EOS can be also combined with the expression for laminar viscosity [88]:

$$\left(\frac{1}{\rho}\nabla \cdot \nabla v\right) = \sum_j \frac{m_j(\mu_i + \mu_j) r_{ij} \cdot \nabla_j W_{ij}}{\rho_i \rho_j (r_{ij}^2 + \varepsilon h^2)} v_{ij} \tag{2.23}$$

and it is used in LAMMPS by invoking

```
pair_style sph/taitwater/morris
pair_coeff I J rho_0 c_0 alpha h
```

2.5.2 Boundary conditions

In the context of fluid dynamics, generally one wants to confine the fluid is a region of space. Although the default LAMMPS build provides several *fix* styles to do that, it is possible to perform an integration only of the energy and local density of SPH particles by invoking

```
fix fix_ID group_ID meso/stationary
```

2.5.3 Velocity-Verlet integration

The numerical method used to integrate Newton's equations of motion is a Velocity-Verlet algorithm [103, 118], and it is commonly implemented in molecular dynamics. There are other methods that can be used, such as the leap frog algorithm or the Beeman's algorithm. Considering a time step Δt, the Velocity-Verlet integration is performed as:

1a) $v_i\left(t+\frac{\Delta t}{2}\right) = v_i(t) + \frac{\Delta t}{2m_i} f_i(t)$

1b) $r_i\left(t+\Delta t\right) = r_i(t) + \Delta t v_i\left(t+\frac{\Delta t}{2}\right)$

2) Calculation of the new forces $f_i(t)\,(t+\Delta t)$

3) $v_i\,(t+\Delta t) = bmv_i\left(t+\frac{\Delta t}{2}\right) + \frac{\Delta t}{2m_i} f_i(t+\Delta t)$

However, as explained in [117], the original algorithm needs to be modified, because when the forces are computed the velocity is lagging the position half a time step. For this reason, an *extrapolated* velocity is computed as:

$$\tilde{v}_i\,(t+\Delta t) = v_i(t) + \frac{\Delta t}{2m_i} f_i(t) \tag{2.24}$$

The atom style *meso* takes into account for this estimate value, and all the SPH calculations are based on it. The complete integration scheme will be:

1a) $v_i\left(t+\frac{\Delta t}{2}\right) = v_i(t) + \frac{\Delta t}{2m_i} f_i(t)$

1b) $\tilde{v}_i\,(t+\Delta t) = v_i(t) + \frac{\Delta t}{2m_i} f_i(t)$

1c) $\rho_i\left(t+\frac{\Delta t}{2}\right) = \rho_i(t) + \frac{\Delta t}{2}\dot{\rho}_i(t)$

1d) $E_i\left(t+\frac{\Delta t}{2}\right) = E_i(t) + \frac{\Delta t}{2}\dot{E}_i(t)$

1e) $r_i\,(t+\Delta t) = r_i(t) + \Delta t v_i\left(t+\frac{\Delta t}{2}\right)$

2) Calculate $f_i(t+\Delta t)$, $\dot{\rho}_i(t+\Delta t)$ and $\dot{E}_i(t+\Delta t)$

3a) $\rho_i\,(t+\Delta t) = \rho_i(t+\frac{\Delta t}{2}) + \frac{\Delta t}{2}\dot{\rho}_i(t+\Delta t)$

3b) $E_i\,(t+\Delta t) = E_i(t+\frac{\Delta t}{2}) + \frac{\Delta t}{2}\dot{E}_i(t+\Delta t)$

3c) $v_i\,(t+\Delta t) = v_i(t+\frac{\Delta t}{2}) + \frac{\Delta t}{2m_i}f_i(t)(t+\Delta t)$

This time integration can be performed in LAMMPS with

```
fix fix_ID group_ID meso
```

2.6 Simulation setup

In the present work, we run our simulations using Theta/ThetaGPU Argonne Leadership Computing Facility (ALCF) computing resources. We used Theta, which is an 11.7-petaflops supercomputer with 4,392 nodes, each of them made of 64 processors. It is intensively used for data analysis, machine learning and numerical simulations. [119] In the current study, we applied a similar setup as in our previous work [83]. We used weakly compressible SPH with the Lucy kernel function, with a smoothing length of 2 µm, and implemented it in LAMMPS [99]. The flow is generated by applying a constant body force to all particles, namely the fluid and the rigid

prolate particles, using periodic boundary conditions (PBCs). Although more sophisticated procedures could be implemented to generate a pressure-driven flow in the channel [120], the ease of handling PBCs in SPH makes the body force solution preferable to other techniques [121, 122]. We computed the Reynolds number as $Re = \frac{v_{\text{ave}} D_h \rho}{\mu}$ where v_{ave} is the average velocity in the channel, D_h is the hydraulic diameter computed as $\frac{2WH}{W+H}$ where W and H are the channel width and height respectively. The density ρ and viscosity μ of the SPH particles constituting the fluid were set to the water's value $1000\frac{\text{kg}}{m^3}$ and $10^{-3}\text{Pa} \cdot \text{s}$ The incompressibility of the flow is enforced by setting the speed of sound c_0 at least 10 times greater than the maximum velocity in the system.

The initial lattice of SPH particles was divided into groups, each one assigned with specific properties. The non-spherical prolate object to be simulated was created by defining an ellipsoidal region whose constituting SPH particle behaves as a single rigid body using the LAMMPS *fix rigid* command. In addition, we took into account for the no-slip boundary conditions, modeling the interaction between fluid particles and the walls following the procedure described by *Morris et al* [88]. An artificial velocity was constructed for the particles at the boundaries, and it was used to compute the viscous forces [88]. The flow develops in the X direction, and it is confined by fixed particles constituting the channel walls. Finally, all the relevant information (position of the center of mass, angular velocity, torque, force, etc.) of the rigid prolate are recorded throughout the simulations. We tracked the entire migration of the particle by dumping the position of the SPH particles and visualizing it with VMD (Visual Molecular Dynamics). [123]

2.6.1 Output visualization

In order to store all the information related to the inertial migration of the shaped particle, the command

```
fix ID group-ID rigid
```

is invoked in LAMMPS. A list of the rigid bodies in the domain is created, and their properties are calculated at the beginning of the run. The main properties include the position of the center of mass at each time step, useful to plot the trajectory of the particle, the linear and angular velocities of the objects, in all three directions, the torque and the forces. The keyword `reinit` is particularly important. In the default setting it is set to `yes`, meaning that at every run, the data structure is re-created. In the present work, since each case has been re-run several times, this keyword was set to `no`, to avoid unwanted shifts in the rigid body coordinates. The output structure for one rigid body is a matrix whose number of rows corresponds to the number of time steps of the simulation. The number of columns is generally 15, corresponding to the x, y, and z components of: the coordinates of the center of mass (COM), COM velocity, force and torque acting on the COM, and the image flags of the COM. All these data are collected in a text file, and then visualized in the Linux shell using *gnuplot*. [124–126] It is a command-line driven graphic utility introduced in 1986, mainly used as a plotting engine.

Moreover, it is possible to generate animations of the simulations. Combined with numerical outputs, these are a valuable instrument to visualize the results and, in case of errors, to understand what might have gone wrong in a prompt way. To do that, the trajectory of the COM is dumped using

```
dump ID group-ID style N file args
```

where `style` is set to `atom`. Dump commands are generally used to store information of specific quantities, related to groups of atoms, every N time steps. A text file containing the LAMMPS trajectory (`"*.lammpstrj"`) is generated, and it can be directly imported in VMD.

VMD is a molecular graphics program released in 1996, written in C^{++}. [123]

It is possible to visualize molecules, atoms, particles and assign them a custom representation style, namely different coloring and rendering modes. VMD contains several additional tools, including its own console, which can be used to add graphical features in the scene. In the present work, this tool was used to include the microchannel edges in the scene, as solid black lines, to assist and improve the final visualization of the particle flowing downstream. The scene itself can be customized changing the background color, perspective, and lighting. It is also possible to modify the trajectories imported in VMD, by adding or deleting frames. Finally, the play back of the trajectory can be controlled by frame increment to modify the animation speed and direction.

2.7 Experimental setup

2.7.1 Device fabrication and high-speed imaging in experiments

Microchannels were designed in a L-shape, so that cross-sectional imaging orthogonal to the flow direction can be setup without difficulty. L-shaped microchannels were fabricated in polydimethylsiloxane (PDMS) using a dry film master. The process for making the dry film master is detailed in our previous work [127]. Briefly, a 150 µm × 50 µm rectangular straight microchannel was patterned on a 3" silicon wafer using dry film (ADEX 50, DJ MicroLaminates

Inc., USA). The microchannel was then replicated in PDMS (Sylgard 184, Dow Corning®, USA) which was bonded to 1" × 3" glass slides (Fisher Scientific, USA) to form sealed devices after O_2 surface plasma treatment (PE-50, Plasma Etch Inc., USA) for 20 s. Inlet and outlet ports were made using a biopsy punch with an outer diameter of 1.5 mm (Ted Pella Inc., USA). Cell sample solution was loaded in a syringe (Norm-Ject®, Air-Tite Inc., USA), which was connected to 1/16" Tygon® tubing (Cole-Palmar, USA) using proper fittings (IDEX Health & Science LLC, USA). The other end of the tubing was secured to the device inlet. A syringe pump (Legato 200, KD Scientific Inc., USA) was used to sustain stable flow rate of 300 µL/min. The microchannel was placed on the stage of an inverted microscope (IX83, Olympus America, USA). Images of cell aggregates inside the microchannel were acquired using a high-speed camera (Mini AX200, Photron USA, Inc.). The frame rate was 25,000 fps and exposure time was 1 µs.

2.7.2 Cell sample preparation

Non-small-cell-lung cancer (NSCLC) cell line A549 was cultured in RPMI 1640 medium supplemented with 10% (v/v) FBS, and 1% (v/v) 100X antibiotic–antimycotic solution in an incubator at 37°C and 5% CO_2. Cell aggregates were formed in the low attachment plates, which were made by coating 12-well plate with anti-adherence solution (Stemcell Technology, Vancouver, Canada) [128]. Anti-adherence solution coated the entire well bottom and excess was removed. Plates treated with anti-adherence solution were placed in a biosafety hood overnight under UV exposure until completely dry. Then, a 1 mL of A549 cell suspension was added into each well at 500K cells/mL. After 2 d of culture, cell aggregates formed and were imaged. Cell

aggregates were fixed using 4% paraformaldehyde (PFA) for 20 min and rinsed in phosphate buffered solution (PBS) before they were run into the microchannel.

CHAPTER 3

RESULTS AND DISCUSSION

Reproduced from [Lauricella, Giuseppe, et al. "Computational study of inertial migration of prolate particles in a straight rectangular channel." Physics of Fluids 34.8 (2022): 082021], with the permission of AIP Publishing

3.1 Validation of SPH model

We first compared values of orbit period with the Jeffery's theory [1]. Jeffery's theory shows that an ellipsoidal particle, in an unbounded linear shear flow, rotates along the so-called Jeffery orbits: a set of infinite orbits that depend on the initial particle orientation. The time required to complete one orbit, the period of rotation, is given as:

$$T = \frac{2\pi}{\gamma} \cdot \left(\frac{1}{\lambda} + \lambda \right)$$

where it is inversely proportional to the shear rate γ, and it increases for higher values of the particle aspect ratio λ. We set up a simulation of a simple shear flow, generated by two parallel plates moving in opposite directions. The prolate particle was located halfway between the two plates and the period of rotation was computed from the simulation. We set the distance of the plates to 80 µm and their velocity to 10 mm/s, 15 mm/s, and 25 mm/s generating 3 different values of shear rate. Our results in Figure 3 are in agreement with the theoretical values. Considering the lowest value of shear rate we used (250 s^{-1}), for a prolate with λ=3,

the theoretical value predicted by the formula is 0.0837 s, the value from our simulation was T=0.0842 s. Similarly, for λ=5, we got T=0.1315 s, versus an expected value of 0.130 s.

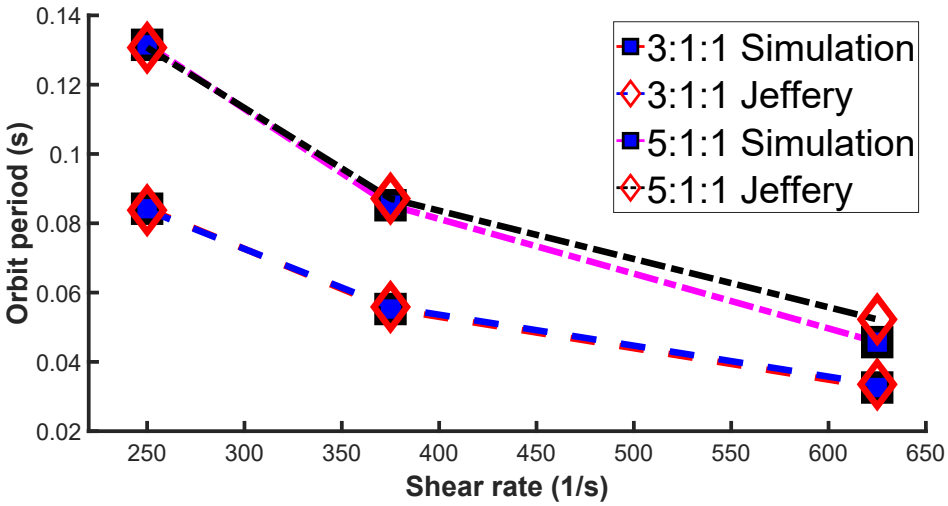

Figure 3: Orbits period from Jeffery's formula [1] (red diamonds) and the result from our SPH simulations in a simple shear flow (blue squares). Higher aspect ratios prolate particles rotate slower, namely 5:1 prolates exhibits higher periods of rotation than the 3:1's. In addition, for increasing values of shear rate, the rotational period decreases for all the ellipsoids.

We also validated our model against an existing numerical study for oblate particles, that employs an immersed boundary method (IBM) in square and rectangular microchannels [2]. We investigated 3 different cases, to test our model in capturing the characteristic behaviors observed in the study. In Figure 4, the cross-sectional view of the channels is shown. The dashed red line is the reference trajectory from Lashgari *et al.* 2017 [2], which overlaps with the

blue and black trajectories from our simulations. We first simulated the motion of an oblate spheroid in a square channel of side H, with a cross-section of 50 µm x 50 µm as shown in Figure 4(b). We set the body force to match the bulk Re=100 used in the study. We tested the first oblate matching the relation $\frac{H}{D_0} = 3.466$, corresponding to a diameter D_0 of 14.4 µm related to our channel dimensions. For this case, Lashgari *et al.* [2] monitored the orientation of the oblate using a unit vector n parallel to the symmetry axis of the particle and then tested different starting positions. We selected one of them and we imposed the same starting orientation, namely $n = [0, 1, 0]$. We obtained the same final focusing position and orientation with SPH. The transitional behavior is a chaotic motion shifting to tumbling, rapidly turning into a log-rolling motion, namely with $n = [1, 0, 0]$. The focusing position was 25 µm and 12 µm away from the wall in the lateral and vertical positions, respectively. Lashgari *et al.* [2] reported that the particle focused on a vertical distance of 0.26H away from the center, corresponding to 12 µm away from the wall for H= 50 µm, thus matching our predicted position. A good match was also obtained in the second case for an oblate particle with a size of 20.6 µm. In this case, Lashgari *et al.* [2] reported a focusing behavior, which was inclined-rolling on the diagonal of the microchannel. The final focusing position was 14.5 µm in both directions. The focusing dynamics and position match the results also in this case. However, we noted that the oblate migrates toward to nearest diagonal from which it was released, as shown in Figure 4c. On the contrary, Lashgari *et al.* [2] reported that the larger oblate migrated to the opposite diagonal, due to an initial acceleration towards to center of the channel. They explained that this is due to the streamwise rotation, that in this case does not decay to zero, as it does for the smaller

particles. We did not observe this behavior, and the discrepancy might be due to the different way in which the solid and fluid phase interaction is handled by the different numerical methods adopted (SPH and IBM) [129]. We observed that the rotation rate increases first and then decrease, following the same trend found in all the other case.

Lastly, since our investigation of prolate particles is in rectangular cross-section, we also tested a case of oblate particles in a rectangular duct of aspect ratio 2 against the result by Lashgari *et al.* [2] as shown Figure 4(a). For this, we kept one side at H = 50 µm and then scaled the top and bottom walls to 100 µm. In addition, the constant body force was chosen so that the resulting bulk Reynolds number was close to 100. We also changed the box length to 200 µm, twice the length used for the square channel. Lashgari *et al.* [2] reported that the distance between the centers of the oblate and the channel is 0.22H, corresponding to a distance 11 µm from the center and 14 µm from the wall. This matches our results, where the oblate focuses in a vertical position oscillating between 13.8 and 14.2 µm from the bottom wall. We also confirmed the logrolling behavior for this case. In Figure 4, the dashed-red line represents the trajectories shown in the paper and are here plotted against our results from SPH simulations. Overall, the initial configuration was set the same as the reference cases for all three simulations. The final focusing behavior and position were confirmed for all cases, except for the bigger oblate, where the focusing position is on the closest diagonal from which it is released.

3.2 Inertial migration of prolate particles in a rectangular microchannel

After the validation of our SPH model, we focused on the transient migration behavior of prolate particles in a straight channel with a rectangular 50 µm x 25 µm cross-section. The

length of the simulation box was set as twice the width of the channel, thus 100 µm, and Re = 50 for all cases. We found that different values of confinement ratio and particle aspect ratio affect the migration dynamics of prolate particles in terms of focusing length and time, period of rotation, angular velocity and rotational motion. These values are reported in Table I and discussed throughout the following sections.

We defined the confinement ratio K for each particle as the largest dimension of the prolate, representing its rotational diameter, divided by the smallest side of the channel (25 µm in our cases). For each value of confinement ratio, we explored three different starting positions and used them for all cases. We located the center of mass of the particle at (10,10), (15,5), and (25,10) initially, thus progressively closer to the center of the channel. We refer to them as starting positions 1,2 and 3. First, we studied the different sizes for the same aspect ratio, and then we made a cross-comparison among different aspect ratios. The starting orientation for all the particles is with their rotational diameter aligned with the flow direction.

In general, the trajectories present oscillations of the center of mass of the particle, due to the rotation of the particles. Even when the particle has reached its final equilibrium position, it moves back and forth around this position in both the lateral and vertical direction.

The general trend we observed is that the lateral focusing position oscillates around the channel center-line for all cases, and the vertical focusing position increases with the size of the particles. For example, for the aspect ratio 3:1:1, the particles focus at 6.8 µm, 7.6 µm, and 8 µm when increasing the confinement ratio. Similarly, we observed a final vertical position of 6.2 µm, 7.4 µm, and 8 µm for the prolate particles with an aspect ratio of 2:1:1. The migration of the center

of mass of the latter is reported in Figure 5, where a zoom on the trajectories is included within the cross-section. For the case of the smallest confinement ratio, the trajectory experiences an overshoot in the lateral position, going beyond the channel mid-line and then going back towards the center, due to inertia. This behavior has been already reported in literature [130].

3.3 Effect of the confinement ratio and particle aspect ratio on the rotational dynamics

We investigated prolate particles of aspect ratios 2:1:1 and 3:1:1, meaning that the longest dimension of the particle, is respectively 2 and 3 times longer than the other dimensions.
The rotational behavior which is mostly observed, throughout all the cases we have investigated, is a transition from a chaotic behavior, namely a combination of the three main motions shown in Figure 2, to kayaking and eventually tumbling. This trend is consistently observed for all starting positions for all cases, except for the starting positions 1 and 2 for the value of K = 0.768 in the 3:1:1 case. For these two cases, the final rotational behavior is logrolling, while the particle starting from position 3 ends up kayaking. As a consequence, the vertical focusing position is 7.2 µm, thus closer to the wall with respect to the same particle starting in position 3, which focuses at 8 µm, as shown in Figure 6. The reason is that, when it is kayaking, the particle is subjected to a greater lift that pushes it away from the wall, like what is reported with the numerical observations by Masaeli *et al.* [13] for tumbling particles. In the cases where the particle logrolls, the repulsive lift is much smaller, therefore the particle gets slightly closer to the nearest wall. Overall, these cases show that the same particle undergoes two

TABLE I: LIST OF THE 18 CASES TESTED IN THE PRESENT INVESTIGATION, INCLUDING PARTICLE DIMENSIONS, ROTATIONAL MODES, PERIOD OF ROTATION, ANGULAR VELOCITY, FOCUSING TIME AND LENGTH.

AR	a (µm)	b (µm)	K	SP (µm)	RM	T (µs)	$\omega_{\min}$ (kHz)	$\omega_{\max}$ (kHz)	$t_f(ms)$	$L_f(mm)$
3:1:1	9.0	3.0	0.36	(10,10)	Tumbling	9	2	42.9	8.5	28.9
				(15,5)		10	2.4	44.5	10	33
				(25,10)		9.5	2.4	44.5	7	23.1
	13.8	4.6	0.55	(10,10)	Tumbling	12	2	34.2	3.8	13.3
				(15,5)		12	2.4	35.8	3	10.2
				(25,10)		11.5	2.4	35.0	3	10.8
	19.2	6.4	0.77	(10,10)	Logrolling	4.5	20.4	22.6	3.8	12.1
				(15,5)	Logrolling	4.5	20.0	23.1	3	9.6
				(25,10)	Kayaking	13	2.4	26.7	6	19.8
2:1:1	6.88	3.44	0.27	(10,10)	Tumbling	5.3	6	42.9	9	27.9
				(15,5)		6.0	6	42.1	9	29.7
				(25,10)		5.8	6	41.4	7	23.1
	10.52	5.26	0.42	(10,10)	Tumbling	6.4	6	35.0	6.0	20.4
				(15,5)		6.4	6	35.0	6.0	19.8
				(15,5)		6.3	6	35.8	6.0	19.8
	14.6	7.3	0.58	(10,10)	Tumbling	7.3	6	31.8	2.2	7.15
				(15,5)		7.4	6	31.8	2	6.6
				(25,10)		7.5	6	31.8	2	6.6

different rotational behaviors, depending on its size and its initial position within the channel cross-section. In Figure 6 we have also plotted how the lateral and vertical positions of the center of mass changes over time and also with respect to the downstream length. These figures provide a sense of the speed of the migration of the particle. First, it rapidly moves towards the equilibrium manifold, represented in a fast variation of the vertical position, followed by a slow migration towards the channel center-line, accordingly to the model presented by Zhou and Papautsky for spherical particles [18]. The equilibrium manifold is an equilibrium region where the particle is equilibrated in the vertical direction, and it experiences a lateral migration towards the equilibrium position. It was described also from Lashgari *et al.* 2017 and other previous works. [131, 132]

The logrolling behavior has not been reported in literature, where the studies converge on the fact that prolate particles always tumble in a Poiseuille flow at moderate Reynolds numbers, similar to the behavior in shear flows. We found that the parameter mainly responsible for the log rolling mode is not the aspect ratio, but the confinement ratio. Indeed, the biggest particles we simulated for both aspect ratios 2:1:1 and 3:1:1, using the same volume, had a different rotational diameter: 14.6 µm and 19.2 µm, respectively. We performed additional simulations where we fixed aspect ratio but inverted values of the confinement ratio. As expected, the 3:1:1 particle that in the original case was logrolling is now tumbling, and the 2:1:1 particle that was tumbling originally is now logrolling. This behavior is due to increase in the rotational diameter.

We identified the threshold value of confinement ratio for the logrolling to occur, assuming that the particle is sufficiently distant from the center, so it can develop all the transitional

behaviors described before. First, since prolate spheroids with d_{rot} = 14.6 µm tumble and those with d_{rot} = 19.2 µm logroll, we ran five additional cases with 3:1:1 particles whose rotational diameter was 15.6, 16.6, 17.6, 18 and 18.6 µm corresponding to confinement ratios of 0.624, 0.664, 0.704, 0.720 and 0.744, respectively. We observed that for the first three cases, the final tumbling motion was confirmed. Confinement ratio K = 0.720 leads to a final kayaking motion and represents an approximate threshold value for a change in the final rotational behavior. Above this value, the particle will logroll. The log-rolling motion of a prolate particle was also confirmed in our experiments in a straight rectangular channel with a cross-section of 150 µm x 50 µm. The flow rate was set to 300 µL/min, corresponding to Re = 50, and the particle was an aggregate of fixed cells, behaving like a rigid body. The aggregate was not perfectly symmetrical, but very close to an axisymmetric 3:1:1 prolate, with a rotational diameter of 50 µm (K=1). We simulated the same experimental conditions and the predicted logrolling motion agrees well with the experimental observation. The comparison between the imaging top view of the channel and the results of our simulation is shown in Figure 7.

3.4 Effect of the initial position and orientation on the rotational behavior

The effect of the particle's initial location and alignment on its migration and focusing behaviors is still not clear for both shear flows and Poiseuille flows. It has been shown that oblate spheroids logroll, regardless of their initial conditions [133], but in the current literature there is no such information for prolate particles. Considering the group of prolate spheroids with K = 0.768, the particle starting in position 3 begins with a tumbling mode and stabilizes in a kayaking motion. On the other hand, we observed that the particles starting in position

1 and 2 exhibit a chaotic rotational behavior initially, but begin kayaking and rolling at the same time while migrating laterally. The dominant orbit progressively flattens while the particle approaches the lateral center-line and the kayaking motion completely transitions into logrolling configuration.

The change in the rotational behaviors when changing the starting position might be also due to the initial orientation of the particle and its location within the parabolic velocity profile in the channel. If the particle is released sufficiently far away from the channel center, it will experience an increasing velocity of the fluid while migrating laterally towards the center, and its transitional behavior will follow the one described before. If the particle is released close to the center, like the starting position 3, its initial configuration will determine the final rotational behavior. At the center, the particle lateral migration is minimal, and it cannot go through the different rotational modes leading to the logrolling. To confirm, we set up an additional simulation in which we released the particle at the starting position 3, but with its rotational diameter perpendicular to the flow direction, namely already in a log rolling set up. The particle migrates downward, reaching a vertical focusing position of 7.2 µm, and exhibits the final log-rolling behavior.

3.5 Effect of particle aspect ratio and confinement ratio on the period of rotation

We also investigated the period of rotation, whose dependency on the size and aspect ratio was still not fully clarified in the previous studies. Hur *et al.* [52] concluded that the orbit period does not depend on the aspect ratio, but on the confinement ratio. On the other hand, Masaeli

et al. [13] reported that the period of rotation increases along with the aspect ratio, following the Jeffery's formula [1]. Computation of this parameter from our simulations reveals that both can be true depending on the particle's aspect ratio and confinement ratio. We observed a higher period of rotation for higher aspect ratios particles and also for increasing values of confinement ratio, with a fixed aspect ratio. However, the magnitude of this difference is greater for distinct aspect ratios and the size contributes to minor changes. Moreover, a particle that is logrolling rotates about 3 times faster than a particle with the same volume that is tumbling.

3.6 Effect of particle aspect ratio and confinement ratio on the angular velocity

Our results show that the angular velocity with respect to the vorticity axis is not constant, but is periodic, with minimum values when the particle is aligned with the flow direction and maximum values when the particle is perpendicular to the top and bottom walls. This characteristic was already reported in several studies [1, 48]. In Figure 8 we show the differences in the angular velocities of particles with a different aspect ratio, but with the same confinement ratio. The number of peaks gives additional information on the number of rotations in the same amount of time, illustrating how the orbit period differs. Figure 8(a) shows two particles undergoing a tumbling motion, while Figure 8(b) shows particles with a higher confinement ratio that stabilize in a logrolling motion. We found that within the same aspect ratio, smaller particles show higher peaks for the maximum angular velocity. The minimum values, when the particle is aligned with the flow direction, change with the aspect ratio. The group of 2:1:1 prolate particles, shown in Figure 9, exhibits a minimum angular velocity close to 2 kHz, whereas it is in the order of 6 kHz for the 3:1:1 group. The minimum and maximum values of the

angular velocity of a logrolling particle are very close, because the oscillations are small and the magnitude almost constant, unlike tumbling particles where the periodicity is non-negligible.

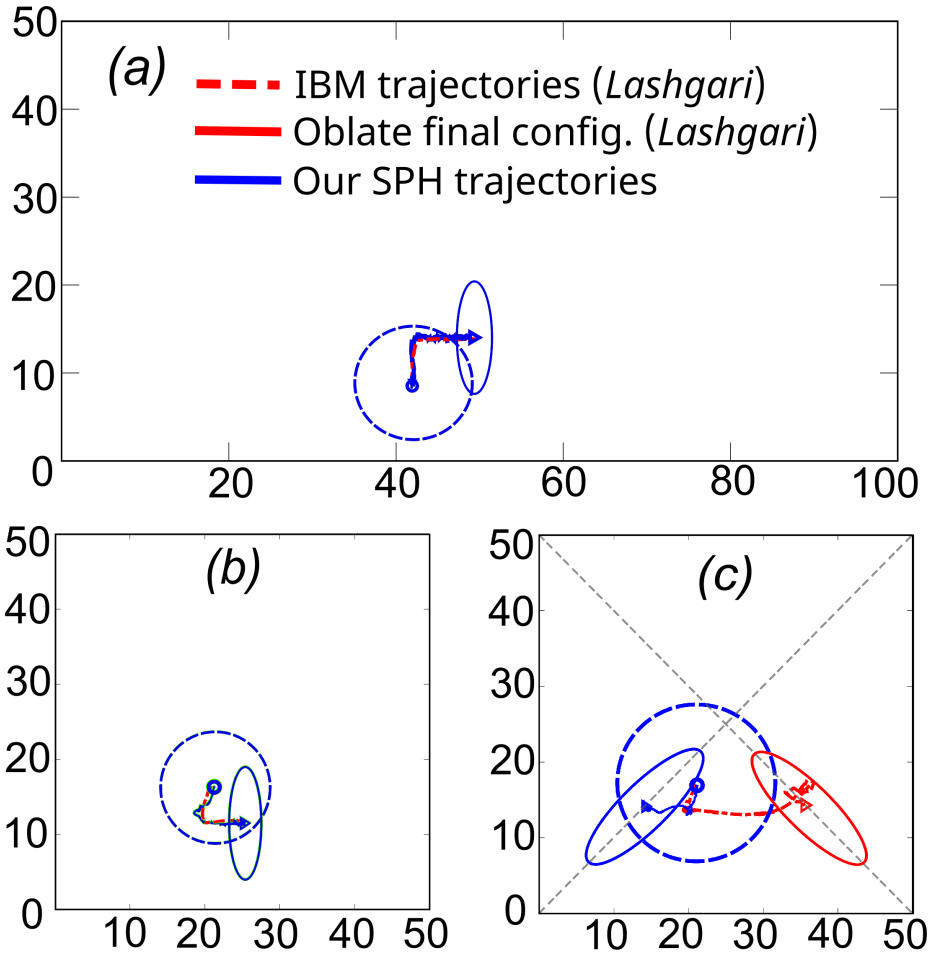

Figure 4: Inertial migration of oblate particles in square and rectangular channels reproduced from Lashgari *et al.* 2017 [2] investigation. The circle and triangle indicate the initial and final position of the center of mass of the oblate spheroid. (b) Oblate in a square channel, with the same diameter of the oblate ellipsoid in the rectangular channel, but starting in position (20 µm, 17 µm). (c) We tested an oblate particle with a radius of 10.3 µm with the same starting position as the other case in the square channel.

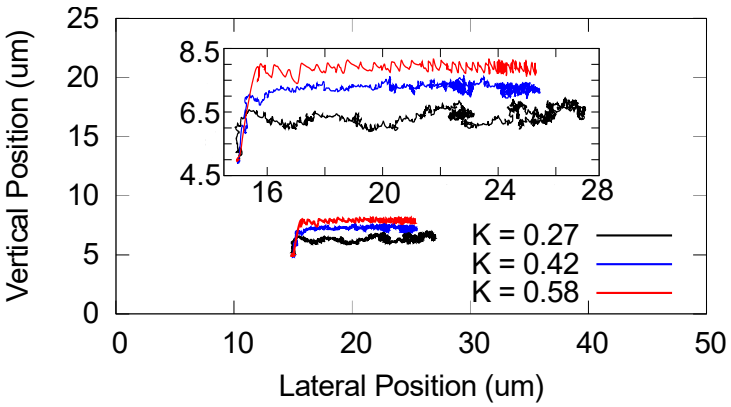

Figure 5: Cross-sectional view of the trajectories for the 2:1:1 prolate spheroids with different values of confinement ratios. The plot shows the particles starting from the same initial position, and it can be noticed that the vertical focusing position is progressively more distant from the bottom wall as the particle size is increased.

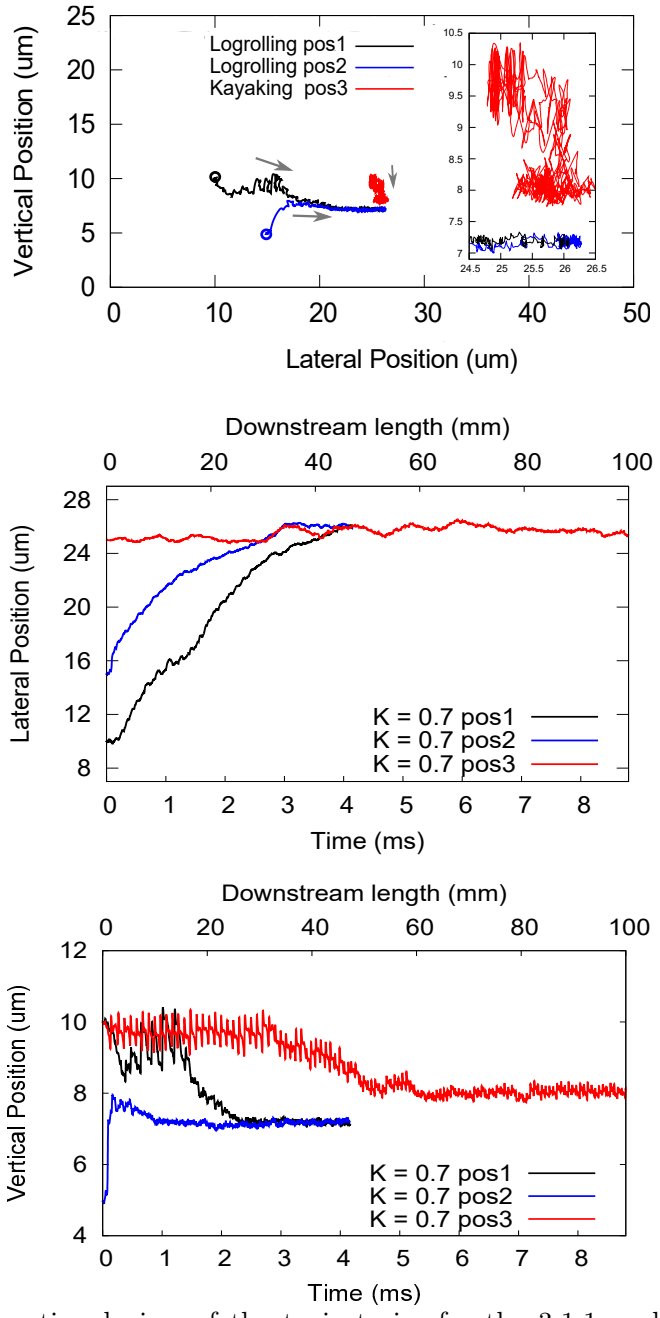

Figure 6: (a) Cross-sectional view of the trajectories for the 3:1:1 prolate spheroids with a value of K = 0.77. (b) Variation of the lateral position of the center of mass versus time and downstream length. (c) Variation of the vertical position of the center of mass versus time and downstream length.

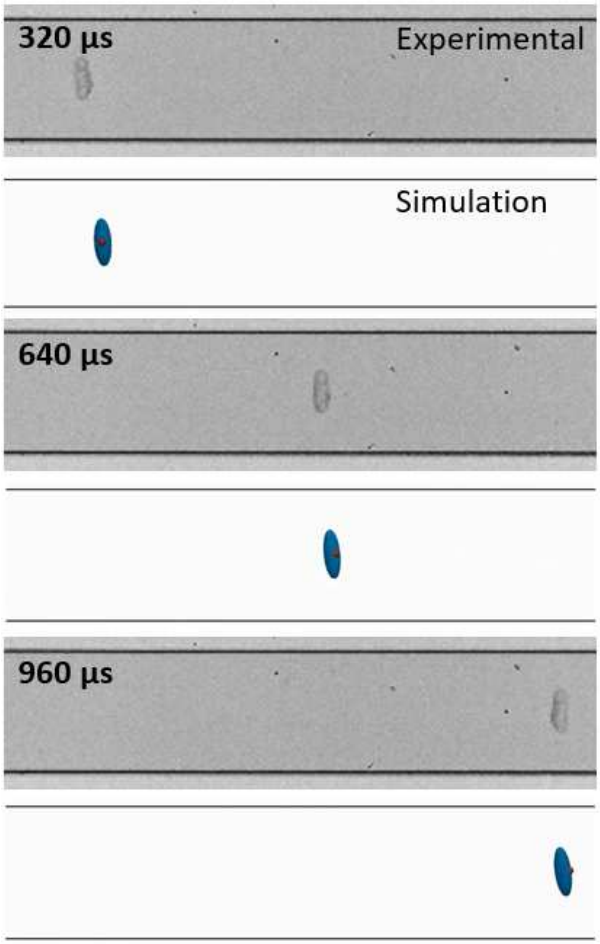

Figure 7: Top-view of a logrolling prolate particle at three different time intervals. The frames from the videos of the simulation and experimental observation have been juxtaposed. The cell aggregate logrolls while moving downstream, and its center of mass is located approximately at the channel center.

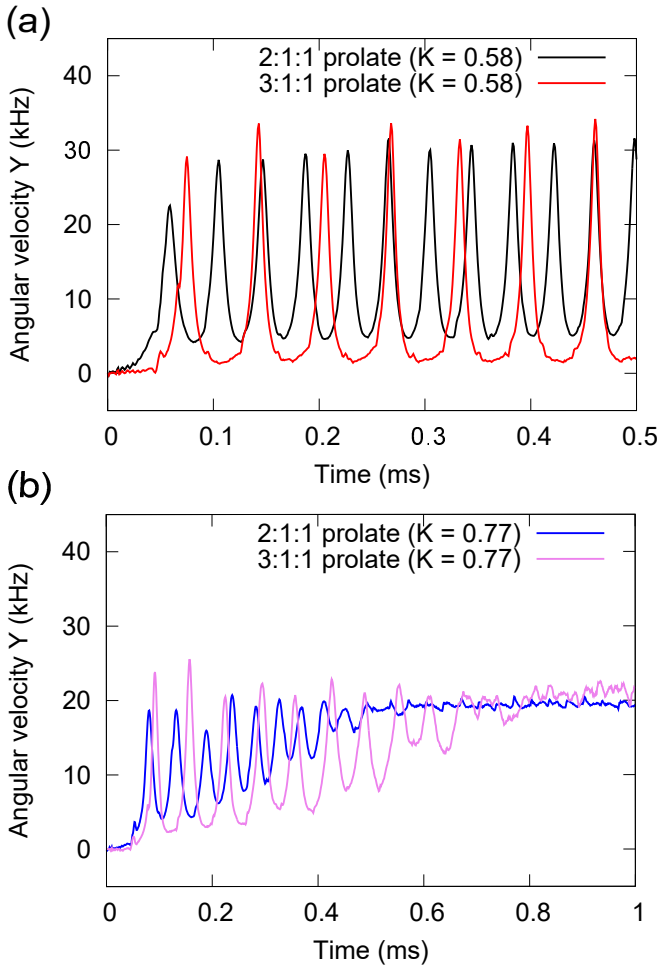

Figure 8: Angular velocity around the y-axis. (a) The frequency of rotation is greater for the lower aspect ratio prolate spheroid. (b) When the rotational diameter is increased, the particles end up log rolling and the angular velocity becomes almost constant, but with slightly different values accordingly to the aspect ratio.

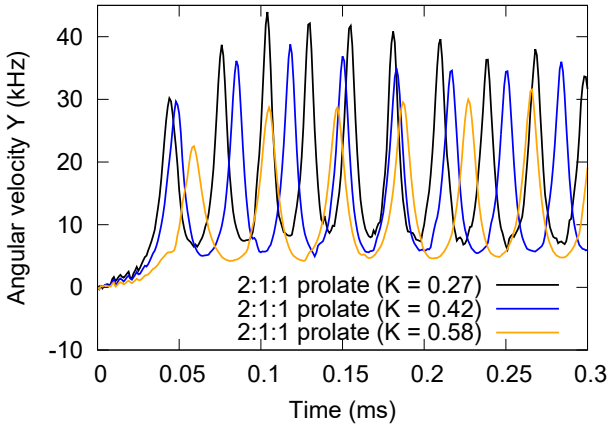

Figure 9: The confinement ratio affects the angular velocity of tumbling particles with the same aspect ratio. The maximum value reached during the rotation is higher for smaller particles, which are also characterized by a higher frequency of rotation. Only a part of the simulation is plotted, but the same trend also extends for the rest of the simulation.

CHAPTER 4

CONCLUSIONS AND FUTURE DEVELOPMENTS

We applied SPH modeling approach to investigate the effects of particle size and shape on its inertial behavior in a straight rectangular duct. We explored behavior of prolate spheroids at Re = 50, testing a range of confinement ratios and 2 values of particle aspect ratios, and examined the migration dynamics within the channel. We not only studied how the focusing position and migration dynamics changes for prolate particles of different sizes and aspect ratios, but also examined the rotational behavior, angular velocity, downstream focusing length, and migration trajectory, mapping their migration dynamics. The general trend is that prolate ellipsoid migrates towards the channel lateral center-line and they assume a final tumbling rotational mode while moving downstream. However, when increasing the particle rotational diameter, thus its blockage ratio, the final rotational behavior can be either kayaking or logrolling, depending on the particle's initial position and orientation. This is the first time this logrolling behavior is reported for prolate spheroids. This new predicted result was confirmed by our microfluidic experiments on cell aggregates with similar shape aspect ratio and confinement ratio. The same particle can undergo a set of transitional behaviors and eventually logrolls if it is sufficiently distant from the center of the channel. If the particle is released near the center, where the fluid velocity is higher, the initial alignment will determine the final mode of rotation. We identified K = 0.72 as the threshold value above which the particle will logroll regardless of its aspect ratio.

In addition, we reported that the orbit period of tumbling particles depends on both the particle's rotational diameter and aspect ratio. Moreover, a prolate spheroid in a tumbling configuration exhibits a period angular velocity, which shows maximum peaks, when the particle is vertically aligned. A prolate particle that is logrolling has an angular velocity that is almost constant, with a value close to the average velocity of a tumbling particle. The result and information provided will be valuable for all the applications of high-throughput separation, sorting, and analysis where particle shape and alignment is relevant.

The research areas that can benefit from this study include, but not limited to, the medical and biological fields, food and environmental technologies. Among the studies that use shape as a biomarker to perform separation and sorting, Li *et al.* successfully developed a device for shape-based separation of a microalga for biomass production, whose shape is a useful indicator for its cell cycle status, environmental condition, and many more [134] . It demonstrates how cells with a different aspect ratio focus on different lateral positions and can passively separate with a throughput of 1,300 cells/sec. Similarly, Liu *et al.* performed a shape based separation with Cerevisiae cells, showing that a variation in shape leads to the migration to different lateral positions and with different velocities [135]. Feng *et al.* used a spiral microchannel to enrich and separate chromosomes from cell debris [121]. Their results show the possibility of separating chromosomes by exploiting their size and aspect ratio: the two factors influencing the final focusing position, thus elution location, in a spiral microchannel. Yuan *et al.* demonstrated for the first time the separation of cyanobacteria using viscoelastic microfluidics, exploiting the effects of different shapes [135]. The emerging studies using this technique suggest the bene-

fit of inertial microfluidics to this kind of application, where particle shape and alignment are relevant. Numerical simulations can provide valuable information on the inertial migration of particles with various shapes by thoroughly exploring and tuning each parameter. Moreover, once the numerical method is validated, it can be used to predict and guide the experimental design. In addition, the simulations provide information that is not accessible experimentally, such as detailed flow and stress fields.

As reported by Behdani *et al.*, shape-based separation is a powerful tool, but the main limiting factors are the lack of a general framework to study the shape effects and the absence of a systematic work in the literature to address the multiple variables that can affect the migration dynamic [136]. By choosing the proper channel cross-section and particle size and aspect ratio, the final focusing behavior can be controlled to obtain the logrolling behavior we reported in this study. This might be useful to allow the optical reading since the particle rotational axis is not changing over time. Also, a prolate ellipsoid could provide more surface area with respect to a spherical droplet or particle. In future work, higher values of the Reynolds number can be investigated to shed more light on the rotational behaviors in this condition, which are still not clear. This approach can be extended to different channel cross-sections and particle shapes to provide some design basis for shape-based separation and interrogation platforms and help their integration into Lab-on-Chip devices.

APPENDICES

Appendix A

AIP PERMISSION TO REUSE OWNED CONTENT

Permission to Reuse Content

Reusing AIP Publishing Content

Permission from AIP Publishing is required to:

- republish content (e.g., excerpts, figures, tables) if you are not the author
- modify, adapt, or redraw materials for another publication
- systematically reproduce content
- store or distribute content electronically
- copy content for promotional purposes

Authors do **not** need permission from AIP Publishing to:

- quote from a publication (please include the material in quotation marks and provide the customary acknowledgment of the source)
- reuse any materials that are licensed under a Creative Commons CC BY license (please format your credit line: "Author names, Journal Titles, Vol.#, Article ID#, Year of Publication; licensed under a Creative Commons Attribution (CC BY) license.")
- reuse your own AIP Publishing article in your thesis or dissertation (please format your credit line: "Reproduced from [FULL CITATION], with the permission of AIP Publishing")
- reuse content that appears in an AIP Publishing journal for republication in another AIP Publishing journal (please format your credit line: "Reproduced from [FULL CITATION], with the permission of AIP Publishing")
- make multiple copies of articles–although you must contact the Copyright Clearance Center (CCC) at www.copyright.com to do this

CITED LITERATURE

1. Jeffery, G. B. and Filon, L. N. G.: The motion of ellipsoidal particles immersed in a viscous fluid. Proceedings of the Royal Society of London. Series A, Containing Papers of a Mathematical and Physical Character, 102(715):161–179, 1922.

2. Lashgari, I., Ardekani, M. N., Banerjee, I., Russom, A., and Brandt, L.: Inertial migration of spherical and oblate particles in straight ducts. Journal of fluid mechanics, 819:540–561, May 25, 2017.

3. Zhang, J., Yan, S., Yuan, D., Alici, G., Nguyen, N.-T., Ebrahimi Warkiani, M., and Li, W.: Fundamentals and applications of inertial microfluidics: a review. Lab on Chip, 16:10–34, 2016.

4. Gossett, D. R., Weaver, W. M., Mach, A., J. Hur, S., Claire, T., Henry, T., Kwong, L. W., Amini, H., and Di Carlo, D.: Label-free cell separation and sorting in microfluidic systems. Analytical and Bioanalytical Chemistry, 397, 2010.

5. Lauricella, G., Zhou, J., Luan, Q., Papautsky, I., and Peng, Z.: Computational study of inertial migration of prolate particles in a straight rectangular channel. Physics of Fluids, 34(8):082021, 2022.

6. Cummins, S. J. and Rudman, M.: An sph projection method. Journal of computational physics, 152(2):584–607, 1999.

7. Zhu, J., Tzeng, T.-R. J., and Xuan, X.: Continuous dielectrophoretic separation of particles in a spiral microchannel. ELECTROPHORESIS, 31(8):1382–1388, 2010.

8. Inglis, D. W., Riehn, R., Austin, R. H., and Sturm, J. C.: Continuous microfluidic immunomagnetic cell separation. Applied Physics Letters, 85(21):5093–5095, 2004.

9. Laurell, T., Petersson, F., and Nilsson, A.: Chip integrated strategies for acoustic separation and manipulation of cells and particles. Chem. Soc. Rev., 36:492–506, 2007.

10. MacDonald, M. P., Spalding, G. C., and Dholakia, K.: Microfluidic sorting in an optical lattice. Nature, 426(6965):1476–4687, 2003.

CITED LITERATURE (continued)

11. Martel, J. M. and Toner, M.: Inertial focusing in microfluidics. Annual review of biomedical engineering, 16(1):371–396, Jul 11, 2014.

12. Zhou, J., Mukherjee, P., Gao, H., Luan, Q., and Papautsky, I.: Label-free microfluidic sorting of microparticles. APL Bioengineering, 3(4):041504, 2019.

13. Masaeli, M., Sollier, E., Amini, H., Mao, W., Camacho, K., Doshi, N., Mitragotri, S., Alexeev, A., and Carlo, D. D.: Continuous inertial focusing and separation of particles by shape. Physical review. X, 2(3):031017, Sep 2012.

14. Amini, H., Lee, W., and Carlo, D. D.: Inertial microfluidic physics. Lab chip, 14(15):2739–2761, Aug 07, 2014.

15. Matas, J., Morris, J., and Guazzelli, E.: Lateral forces on a sphere. Oilamp;gas science and technology , 59(1):59–70, Jan 2004.

16. Segré, G. and Silberberg, A.: Radial particle displacements in poiseuille flow of suspensions. Nature, 189:209–210, 1961.

17. Carlo, D. D., Irimia, D., Tompkins, R. G., and Toner, M.: Continuous inertial focusing, ordering, and separation of particles in microchannels. Proceedings of the National Academy of Sciences - PNAS, 104(48):18892–18897, Nov 27, 2007.

18. Zhou, J. and Papautsky, I.: Fundamentals of inertial focusing in microchannels. Lab Chip, 13:1121–1132, 2013.

19. Rubinow, S. I. and Keller, J. B.: The transverse force on a spinning sphere moving in a viscous fluid. Journal of Fluid Mechanics, 11(3):447–459, 1961.

20. Matas, Jp., Morris, Jf., and Guazzelli, E.: Lateral forces on a sphere. Oil & Gas Science and Technology - Rev. IFP, 59(1):59–70, 2004.

21. Lee, M. G., Choi, S., and Park, J.-K.: Rapid laminating mixer using a contraction-expansion array microchannel. Applied Physics Letters, 95(5):051902, 2009.

22. Zhang, J., Li, M., Li, W. H., and Alici, G.: Inertial focusing in a straight channel with asymmetrical expansion–contraction cavity arrays using two secondary flows. Journal of Micromechanics and Microengineering, 23(8):085023, jul 2013.

CITED LITERATURE (continued)

23. Zhou, Z., Chen, Y., Zhu, S., Liu, L., Ni, Z., and Xiang, N.: Inertial microfluidics for high-throughput cell analysis and detection: a review. Analyst, 146:6064–6083, 2021.

24. Hanzard, P.-H., Godin, T., Idlahcen, S., Rozé, C., and Hideur, A.: Real-time tracking of single shockwaves via amplified time-stretch imaging. Applied Physics Letters, 112(16):161106, 2018.

25. Tavassoli, H., Rorimpandey, P., Kang, Y. C., Carnell, M., Brownlee, C., Pimanda, J. E., Chan, P. P., and Chandrakanthan, V.: Label-free isolation and single cell biophysical phenotyping analysis of primary cardiomyocytes using inertial microfluidics. Small, 17(8):2006176, 2021.

26. Sun, J., Li, M., Liu, C., Zhang, Y., Liu, D., Liu, W., Hu, G., and Jiang, X.: Double spiral microchannel for label-free tumor cell separation and enrichment. Lab Chip, 12:3952–3960, 2012.

27. Jimenez, M., Miller, B., and Bridle, H. L.: Efficient separation of small microparticles at high flowrates using spiral channels: Application to waterborne pathogens. Chemical Engineering Science, 157:247–254, 2017. 12th International Conference on Gas-Liquid and Gas-Liquid-Solid Reactor Engineering.

28. Rodríguez-Pena, A., Armendariz, E., Oyarbide, A., Morales, X., Ortiz-Espinosa, S., Ruiz-Fernández de Córdoba, B., Cochonneau, D., Cornago, I., Heymann, D., Argemi, J., D'Avola, D., Sangro, B., Lecanda, F., Pio, R., Cortés-Domínguez, I., and Ortiz-de Solórzano, C.: Design and validation of a tunable inertial microfluidic system for the efficient enrichment of circulating tumor cells in blood. Bioengineering & Translational Medicine, n/a(n/a):e10331.

29. Shiriny, A. and Bayareh, M.: Inertial focusing of ctcs in a novel spiral microchannel. Chemical Engineering Science, 229:116102, 2021.

30. Xu, X., Huang, X., Sun, J., Wang, R., Yao, J., Han, W., Wei, M., Chen, J., Guo, J., Sun, L., and Yin, M.: Recent progress of inertial microfluidic-based cell separation. Analyst, 146:7070–7086, 2021.

31. Hassan, M. M., Ranzoni, A., and Cooper, M. A.: A nanoparticle-based method for culture-free bacterial dna enrichment from whole blood. Biosensors and Bioelectronics, 99:150–155, 2018.

CITED LITERATURE (continued)

32. Hadikhani, P., Hashemi, S. M. H., Balestra, G., Zhu, L., Modestino, M. A., Gallaire, F., and Psaltis, D.: Inertial manipulation of bubbles in rectangular microfluidic channels. Lab Chip, 18:1035–1046, 2018.

33. Y., G., Y., J., P., W., and C., S.: Progress of inertial microfluidics in principle and application. Sensors, 18:1035–1046, 2018.

34. Nawaz, A. A., Zhang, X., Mao, X., Rufo, J., Lin, S.-C. S., Guo, F., Zhao, Y., Lapsley, M., Li, P., McCoy, J. P., Levine, S. J., and Huang, T. J.: Sub-micrometer-precision, three-dimensional (3d) hydrodynamic focusing via "microfluidic drifting". Lab Chip, 14:415–423, 2014.

35. Syverud, B. C., Lin, E., Nagrath, S., and Larkin, L. M.: Label-free, high-throughput purification of satellite cells using microfluidic inertial separation. Tissue Engineering Part C: Methods, 24(1):32–41, 2018. PMID: 28946802.

36. Wang, L. and Dandy, D. S.: A microfluidic concentrator for cyanobacteria harvesting. Algal Research, 26:481–489, 2017.

37. Schoeman, R. M., Kemna, E. W., Wolbers, F., and van den Berg, A.: High-throughput deterministic single-cell encapsulation and droplet pairing, fusion, and shrinkage in a single microfluidic device. ELECTROPHORESIS, 35(2-3):385–392, 2014.

38. Zhang, J., Yuan, D., Zhao, Q., Yan, S., Tang, S.-Y., Tan, S. H., Guo, J., Xia, H., Nguyen, N.-T., and Li, W.: Tunable particle separation in a hybrid dielectrophoresis (dep)-inertial microfluidic device. Sensors and Actuators B: Chemical, 267:14–25, 2018.

39. Wang, X., Gao, H., Dindic, N., Kaval, N., and Papautsky, I.: A low-cost, plug-and-play inertial microfluidic helical capillary device for high-throughput flow cytometry. Biomicrofluidics, 11(1):014107, 2017.

40. Mohamed Yousuff, C., B Hamid, N. H., Kamal Basha, I. H., and Wei Ho, E. T.: Output channel design for collecting closely-spaced particle streams from spiral inertial separation devices. AIP Advances, 7(8):085004, 2017.

41. Nam, J., Jang, W. S., and Lim, C. S.: Micromixing using a conductive liquid-based focused surface acoustic wave (cl-fsaw). Sensors and Actuators B: Chemical, 258:991–997, 2018.

CITED LITERATURE (continued)

42. Martel, J. M. and Toner, M.: Inertial focusing in microfluidics. Annual Review of Biomedical Engineering, 16(1):371–396, 2014. PMID: 24905880.

43. Li, P., Mao, Z., Peng, Z., Zhou, L., Chen, Y., Huang, P.-H., Truica, C. I., Drabick, J. J., El-Deiry, W. S., Dao, M., Suresh, S., and Huang, T. J.: Acoustic separation of circulating tumor cells. Proceedings of the National Academy of Sciences, 112(16):4970–4975, 2015.

44. Li, X., Tao, Y., Lee, D.-H., Wickramasinghe, H. K., and Lee, A. P.: In situ mrna isolation from a microfluidic single-cell array using an external afm nanoprobe. Lab Chip, 17:1635–1644, 2017.

45. Ren, H., Zhu, Z., Xiang, N., Wang, H., Zheng, T., An, H., Nguyen, N.-T., and Zhang, J.: Multiplexed serpentine microchannels for high-throughput sorting of disseminated tumor cells from malignant pleural effusion. Sensors and Actuators B: Chemical, 337:129758, 2021.

46. Jiang, D., Ni, C., Tang, W., and Xiang, N.: Numerical simulation of elasto-inertial focusing of particles in straight microchannels. Journal of Physics D: Applied Physics, 54(6):065401, nov 2020.

47. Cruz, J., Graells, T., Walldén, M., and Hjort, K.: Inertial focusing with sub-micron resolution for separation of bacteria. Lab Chip, 19:1257–1266, 2019.

48. Bretherton, F. P.: The motion of rigid particles in a shear flow at low reynolds number. Journal of Fluid Mechanics, 14(2):284–304, 1962.

49. Tohme, T., Magaud, P., and Baldas, L.: Transport of non-spherical particles in square microchannel flows: A review. Micromachines (Basel), 12(3):277, Mar 07, 2021.

50. Huang, Y., Marson, R. L., and Larson, R. G.: Inertial migration of neutrally buoyant prolate and oblate spheroids in plane poiseuille flow using dissipative particle dynamics simulations. Computational materials science, 162:178–185, May 2019.

51. Pan, T.-W., Chang, C.-C., and Glowinski, R.: On the motion of a neutrally buoyant ellipsoid in a three-dimensional poiseuille flow. Computer methods in applied mechanics and engineering, 197(25):2198–2209, 2008.

52. Hur, S. C., Choi, S.-E., Kwon, S., and Carlo, D. D.: Inertial focusing of non-spherical microparticles. Applied Physics Letters, 99(4), 2011.

CITED LITERATURE (continued)

53. Bazaz, S. R., Mashhadian, A., Ehsani, A., Saha, S. C., Krüger, T., and Warkiani, M. E.: Computational inertial microfluidics: a review. Lab on a chip, 20(6):1023–1048, Mar 17, 2020.

54. Golub, G. H. and Ortega, J. M.: Scientific computing: an introduction with parallel computing. Elsevier, 2014.

55. R.D.Richtmyer: Difference methods for initial-value problems. Interscience Pub. Inc., 13(10):657–658, 1958.

56. Moin, P.: Fundamentals of Engineering Numerical Analysis. Cambridge University Press, 2 edition, 2010.

57. Saffman, P. G.: The lift on a small sphere in a slow shear flow. Journal of Fluid Mechanics, 22(2):385–400, 1965.

58. Constantin, P. and Foias, C.: Navier-stokes equations. University of Chicago Press, 2020.

59. Peskin, C. S.: Flow patterns around heart valves: A numerical method. Journal of Computational Physics, 10(2):252–271, 1972.

60. Peskin, C. S.: The immersed boundary method. Acta Numerica, 11:479–517, 2002.

61. Mittal, R. and Iaccarino, G.: Immersed boundary methods. Annual Review of Fluid Mechanics, 37(1):239–261, 2005.

62. Uhlmann, M.: An immersed boundary method with direct forcing for the simulation of particulate flows. Journal of Computational Physics, 209:448–476, 11 2005.

63. Breugem, W.-P.: A second-order accurate immersed boundary method for fully resolved simulations of particle-laden flows. Journal of Computational Physics, 231:4469–4498, 05 2012.

64. Luo, H.: Immersed boundary method. pages 805–808, 2008.

65. McNamara, G. R. and Zanetti, G.: Use of the boltzmann equation to simulate lattice-gas automata. Phys. Rev. Lett., 61:2332–2335, Nov 1988.

66. Hardy, J., Pomeau, Y., and de Pazzis, O.: Time evolution of a two-dimensional classical lattice system. Phys. Rev. Lett., 31:276–279, Jul 1973.

CITED LITERATURE (continued)

67. Arumuga Perumal, D. and Dass, A. K.: A review on the development of lattice boltzmann computation of macro fluid flows and heat transfer. Alexandria Engineering Journal, 54(4):955–971, 2015.

68. He, X. and Luo, L.-S.: Theory of the lattice boltzmann method: From the boltzmann equation to the lattice boltzmann equation. Phys. Rev. E, 56:6811–6817, Dec 1997.

69. Perumal, D. A. and Dass, A.: Simulation of flow in two-sided lid-driven square cavities by the lattice Boltzmann method, volume 59. WIT Press, 2008.

70. Krueger, T., Kusumaatmaja, H., Kuzmin, A., Shardt, O., Silva, G., and Viggen, E.: The Lattice Boltzmann Method: Principles and Practice. Graduate Texts in Physics. Springer, 2016.

71. Succi, S.: The lattice Boltzmann equation: for fluid dynamics and beyond. Oxford university press, 2001.

72. Niedoba, P., Cermák, L., and Jícha, M.: Meshfree methods for computational fluid dynamics. EPJ Web of Conferences, 45:01068, 2013.

73. Mendez, S. F.: Mesh-free methods and finite elements friend or foe?. 2001.

74. Liu, G.: Meshfree Methods: Moving Beyond the Finite Element Method, Second Edition. CRC Press LLC, 2018.

75. Lucy, L. B.: A numerical approach to the testing of the fission hypothesis. astron. j. 82,1013–1024 (1977). Astronomical Journal.

76. Gingold, R. A. and Monaghan, J. J.: Smoothed particle hydrodynamics: theory and application to non-spherical stars. Monthly Notices of the Royal Astronomical Society, 181(3):375–389, 12 1977.

77. Qian, D., Zhou, X., Daxini, S. D., and Prajapati, J. M.: A review on recent contribution of meshfree methods to structure and fracture mechanics applications. The Scientific World Journal, 2014.

78. Liu, G. R. and Liu, M. B.: Smoothed Particle Hydrodynamics. WORLD SCIENTIFIC, 2003.

CITED LITERATURE (continued)

79. Monaghan, J. J.: Smoothed particle hydrodynamics. Reports on progress in physics, 68(8):1703, 2005.

80. Gingold, R. and Monaghan, J.: Kernel estimates as a basis for general particle methods in hydrodynamics. Journal of Computational Physics, 46(3):429–453, 1982.

81. Hoover, W.: Isomorphism linking smooth particles and embedded atoms. Physica A-statistical Mechanics and Its Applications - PHYSICA A, 260:244–254, 11 1998.

82. Hoover, W. G., Hoover, C. G., and Merritt, E. C.: Smooth-particle applied mechanics: Conservation of angular momentum with tensile stability and velocity averaging. Phys. Rev. E, 69:016702, Jan 2004.

83. Zhou, J., Peng, Z., and Papautsky, I.: Mapping inertial migration in the cross section of a microfluidic channel with high-speed imaging. Microsystemsamp;nanoengineering , 6(1):105, Jan 01, 2020.

84. Hosseini, S. M. and Feng, J. J.: Pressure boundary conditions for computing incompressible flows with sph. Journal of Computational Physics, 230(19):7473–7487, 2011.

85. Eckart, C.: Variation principles of hydrodynamics. The Physics of Fluids, 3(3):421–427, 1960.

86. Liu, G.-R. and Liu, M. B.: Smoothed particle hydrodynamics: a meshfree particle method. World scientific, 2003.

87. Monaghan, J. J.: Smoothed particle hydrodynamics. Annual Review of Astronomy and Astrophysics, 30(1):543–574, 1992.

88. Morris, J. P., Fox, P. J., and Zhu, Y.: Modeling low reynolds number incompressible flows using sph. Journal of computational physics, 136(1):214–226, Sep 01, 1997.

89. Monaghan, J. J. and Kos, A.: Solitary waves on a cretan beach. Journal of waterway, port, coastal, and ocean engineering, 125(3):145–155, 1999.

90. Hughes, J. P. and Graham, D. I.: Comparison of incompressible and weakly-compressible sph models for free-surface water flows. Journal of Hydraulic Research, 48(sup1):105–117, 2010.

CITED LITERATURE (continued)

91. Shadloo, M. S., Zainali, A., Sadek, S. H., and Yildiz, M.: Improved incompressible smoothed particle hydrodynamics method for simulating flow around bluff bodies. Computer Methods in Applied Mechanics and Engineering, 200(9):1008–1020, 2011.

92. Shadloo, M. S., Zainali, A., Yildiz, M., and Suleman, A.: A robust weakly compressible sph method and its comparison with an incompressible sph. International Journal for Numerical Methods in Engineering, 89(8):939–956, 2012.

93. Violeau, D. and Leroy, A.: On the maximum time step in weakly compressible sph. Journal of Computational Physics, 256:388–415, 2014.

94. Almasi, G. S. and Gottlieb, A.: Highly parallel computing. Benjamin-Cummings Publishing Co., Inc., 1994.

95. Skillicorn, D. B. and Talia, D.: Models and languages for parallel computation. ACM Comput. Surv., 30(2):123–169, jun 1998.

96. Flynn, M.: Very high-speed computing systems. Proceedings of the IEEE, 54(12):1901–1909, 1966.

97. Grama, A., Kumar, V., Gupta, A., and Karypis, G.: Introduction to Parallel Computing. Pearson Education. Addison-Wesley, 2003.

98. Hager, G. and Wellein, G.: Introduction to high performance computing for scientists and engineers. CRC Press, 2010.

99. Thompson, A. P., Aktulga, H. M., Berger, R., Bolintineanu, D. S., Brown, W. M., Crozier, P. S., in 't Veld, P. J., Kohlmeyer, A., Moore, S. G., Nguyen, T. D., Shan, R., Stevens, M. J., Tranchida, J., Trott, C., and Plimpton, S. J.: LAMMPS - a flexible simulation tool for particle-based materials modeling at the atomic, meso, and continuum scales. Comp. Phys. Comm., 271:108171, 2022.

100. Phillips, J. C., Hardy, D. J., Maia, J. D. C., Stone, J. E., Ribeiro, J. V., Bernardi, R. C., Buch, R., Fiorin, G., Hénin, J., Jiang, W., McGreevy, R., Melo, M. C. R., Radak, B. K., Skeel, R. D., Singharoy, A., Wang, Y., Roux, B., Aksimentiev, A., Luthey-Schulten, Z., Kalé, L. V., Schulten, K., Chipot, C., and Tajkhorshid, E.: Scalable molecular dynamics on cpu and gpu architectures with namd. The Journal of Chemical Physics, 153(4):044130, 2020.

CITED LITERATURE (continued)

101. Abraham, M. J., Murtola, T., Schulz, R., Páll, S., Smith, J. C., Hess, B., and Lindahl, E.: Gromacs: High performance molecular simulations through multi-level parallelism from laptops to supercomputers. SoftwareX, 1-2:19–25, 2015.

102. Brooks, B. R., Brooks III, C. L., Mackerell Jr., A. D., Nilsson, L., Petrella, R. J., Roux, B., Won, Y., Archontis, G., Bartels, C., Boresch, S., Caflisch, A., Caves, L., Cui, Q., Dinner, A. R., Feig, M., Fischer, S., Gao, J., Hodoscek, M., Im, W., Kuczera, K., Lazaridis, T., Ma, J., Ovchinnikov, V., Paci, E., Pastor, R. W., Post, C. B., Pu, J. Z., Schaefer, M., Tidor, B., Venable, R. M., Woodcock, H. L., Wu, X., Yang, W., York, D. M., and Karplus, M.: Charmm: The biomolecular simulation program. Journal of Computational Chemistry, 30(10):1545–1614, 2009.

103. Verlet, L.: Computer "experiments" on classical fluids. i. thermodynamical properties of lennard-jones molecules. Phys. Rev., 159:98–103, Jul 1967.

104. Meloni, S., Rosati, M., and Colombo, L.: Efficient particle labeling in atomistic simulations. The Journal of Chemical Physics, 126(12):121102, 2007.

105. Muser, M. H., Sukhomlinov, S. V., and Pastewka, L.: Interatomic potentials: Achievements and challenges. arXiv preprint arXiv:2204.09563, 2022.

106. Lennard-Jones, J. E.: Cohesion. Proceedings of the Physical Society, 43(5):461–482, sep 1931.

107. Sagui, C. and Darden, T. A.: Molecular dynamics simulations of biomolecules: Long-range electrostatic effects. Annual Review of Biophysics and Biomolecular Structure, 28(1):155–179, 1999. PMID: 10410799.

108. Hockney, R. W. and Eastwood, J. W.: Computer simulation using particles. crc Press, 2021.

109. Pollock, E. and Glosli, J.: Comments on p3m, fmm, and the ewald method for large periodic coulombic systems. Computer Physics Communications, 95(2):93–110, 1996.

110. Darden, T., York, D., and Pedersen, L.: Particle mesh ewald: An nlog(n) method for ewald sums in large systems. The Journal of Chemical Physics, 98(12):10089–10092, 1993.

111. Husic, B. E. and Pande, V. S.: Markov state models: From an art to a science. Journal of the American Chemical Society, 140(7):2386–2396, 2018. PMID: 29323881.

CITED LITERATURE (continued)

112. Grime, J. M. A. and Voth, G. A.: Highly scalable and memory efficient ultra-coarse-grained molecular dynamics simulations. Journal of Chemical Theory and Computation, 10(1):423–431, 2014. PMID: 26579921.

113. Stuart, S. J., Tutein, A. B., and Harrison, J. A.: A reactive potential for hydrocarbons with intermolecular interactions. The Journal of Chemical Physics, 112(14):6472–6486, 2000.

114. Daw, M. S. and Baskes, M. I.: Embedded-atom method: Derivation and application to impurities, surfaces, and other defects in metals. Physical Review B, 29:6443–6453, 1984.

115. Kremer, K. and Grest, G. S.: Dynamics of entangled linear polymer melts: a molecular-dynamics simulation. The Journal of Chemical Physics, 92(8):5057–5086, 1990.

116. Baschnagel, J., Binder, K., Doruker, P., Gusev, A. A., Hahn, O., Kremer, K., Mattice, W. L., Müller-Plathe, F., Murat, M., Paul, W., et al.: Bridging the gap between atomistic and coarse-grained models of polymers: Status and perspectives. Viscoelasticity, atomistic models, statistical chemistry, pages 41–156, 2000.

117. Ganzenmüller, G. C., Steinhauser, M. O., and Van Liedekerke, P.: The implementation of smooth particle hydrodynamics in lammps. Katholieke Universiteit, Leuven, 1:1–26, 2011.

118. Swope, W. C., Andersen, H. C., Berens, P. H., and Wilson, K. R.: A computer simulation method for the calculation of equilibrium constants for the formation of physical clusters of molecules: Application to small water clusters. The Journal of Chemical Physics, 76(1):637–649, 1982.

119. Fahey, M. R., Alexeev, Y., Allcock, B., Allen, B. S., Balakrishnan, R., Benali, A., Booker, L., Boyle, A., Briggs, L., Brooks, E., et al.: Theta and mira at argonne national laboratory. In Contemporary High Performance Computing, pages 31–61. CRC Press, 2019.

120. Lykov, K., Li, X., Lei, H., Pivkin, I. V., and Karniadakis, G. E.: Inflow/outflow boundary conditions for particle-based blood flow simulations: Application to arterial bifurcations and trees. PLoS computational biology, 11(8):e1004410, Aug 2015.

121. Wu, T. and Feng, J. J.: Simulation of malaria-infected red blood cells in microfluidic channels: Passage and blockage.

CITED LITERATURE (continued)

122. Yazdani, A., Deng, M., Caswell, B., and Karniadakis, G. E.: Flow in complex domains simulated by dissipative particle dynamics driven by geometry-specific body-forces. Journal of Computational Physics, 305:906–920, 2016.

123. Humphrey, W., Dalke, A., and Schulten, K.: Vmd: Visual molecular dynamics. Journal of Molecular Graphics, 14(1):33, -02 1996.

124. Janert, P. K.: Gnuplot in action: understanding data with graphs. Simon and Schuster, 2016.

125. Racine, J.: gnuplot 4.0: a portable interactive plotting utility. 2006.

126. Williams, T., Kelley, C., Lang, R., Kotz, D., and Campbell, J.: 1 gnuplot. 2004.

127. Mukherjee, P., Nebuloni, F., Gao, H., Zhou, J., and Papautsky, I.: Rapid prototyping of soft lithography masters for microfluidic devices using dry film photoresist in a non-cleanroom setting. Micromachines, 10(3), 2019.

128. Luan, Q., Becker, J. H., Macaraniag, C., Massad, M. G., Zhou, J., Shimamura, T., and Papautsky, I.: Non-small cell lung carcinoma spheroid models in agarose microwells for drug response studies. Lab Chip, pages –, 2022.

129. Rakhsha, M., Kees, C. E., and Negrut, D.: Lagrangian vs. eulerian: An analysis of two solution methods for free-surface flows and fluid solid interaction problems. Fluids, 6(12), 2021.

130. Feng, J., Hu, H. H., and Joseph, D. D.: Direct simulation of initial value problems for the motion of solid bodies in a newtonian fluid part 1. sedimentation. Journal of Fluid Mechanics, 261:95–134, 1994.

131. Prohm, C. and Stark, H.: Feedback control of inertial microfluidics using axial control forces. Lab Chip, 14:2115–2123, 2014.

132. Liu, C., Hu, G., Jiang, X., and Sun, J.: Inertial focusing of spherical particles in rectangular microchannels over a wide range of reynolds numbers. Lab Chip, 15:1168–1177, 2015.

133. Nizkaya, T. V., Gekova, A. S., Harting, J., Asmolov, E. S., and Vinogradova, O. I.: Inertial migration of oblate spheroids in a plane channel. Physics of Fluids, 32(11):112017, 2020.

CITED LITERATURE (continued)

134. Li, M., Muñoz, H. E., Goda, K., and Carlo, D. D.: Shape-based separation of microalga euglena gracilis using inertial microfluidics. Scientific Reports, 7(1), -09-07 2017.

135. Liu, P., Liu, H., Yuan, D., Jang, D., Yan, S., and Li, M.: Separation and enrichment of yeast saccharomyces cerevisiae by shape using viscoelastic microfluidics. Analytical Chemistry, 93(3):1586, -12-08 2020.

136. Behdani, B., Monjezi, S., Carey, M. J., Weldon, C. G., Zhang, J., Wang, C., and Park, J.: Shape-based separation of micro-/nanoparticles in liquid phases. Biomicrofluidics, 12(5):051503, Sep 2018.

VITA

NAME	Giuseppe Lauricella
EDUCATION	
February 2021 - Present	Master of Science in BioEngineering (BioE), University of Illinois at Chicago, USA
September 2020 - July 2022	Master Degree in Biomedical Engineering (BE), Politecnico di Milano, Italy
September 2017 - July 2020	Bachelor Degree in Biomedical Engineering (BE), Politecnico di Milano, Italy
LANGUAGE SKILLS	
Italian	Native speaker
English	Full working proficiency
EXPERIENCE	
August 2021 - Present	Research Assistant at UIC
PUBLICATIONS	
Sensors	Alessandra Angelucci, Matteo Cavicchioli, Ilaria A Cintorrino, Giuseppe Lauricella, Chiara Rossi, Sara Strati, Andrea Aliverti. Smart textiles and sensorized garments for physiological monitoring: A review of available solutions and techniques. *2021 MDPI Sensors vol. 21, issue 3, DOI: 10.3390/s21030814.*
Physics of Fluids	Giuseppe Lauricella, Jian Zhou, Qiyue Luan, Ian Papautsky, Zhangli Peng. Computational study of inertial migration of prolate particles in a straight rectangular channel. *2022 AIP Publishing LLC Physics of Fluids, vol. 34, issue 8, DOI: 10.1063/5.0100963*